Quarterly Report for

# January - March 2002

# Stanford Geothermal Program

DE-FG07-99ID13763

# Table of Contents

# 1. STEAM-WATER RELATIVE PERMEABILITY IN FRACTURES

This project is being conducted by Research Assistant Chih-Ying Chen, Research Associate Kewen Li and Prof. Roland Horne. The goal is to gain better understanding of steam-water transport through fractured media and determine the behavior of relative permeability in fractures. According to the preliminary results, the behavior of steam-water flow is different from that of air-water flow.

## 1.1 THEORETICAL BACKGROUND

Multiphase flow is an important behavior of geothermal reservoirs, which are complex systems of porous and fractured media. Complete understanding of geothermal fluid flow requires knowledge of flow in both media. Normally, fractures are the main conduits for fluid transport in geothermal reservoirs. In geothermal reservoirs, the fluids, steam and water, are both derived from the same substance but in different phases. The phase change during steam-water flow is a physical phenomenon that does not occur in the multiphase flow of distinct fluids such as air and water, hence the multiphase flow properties are likely to differ. At present, the governing flow mechanism for boiling multiphase flow in fractures is still undetermined. There are two approaches commonly used to model multiphase flow in fractures, the porous medium approach and the equivalent homogeneous single-phase approach.

The porous medium approach treats fractures as connected two-dimensional porous media. In this model, a pore space occupied by one phase is not available for flow for the other phase. A phase can move from one position to another only upon establishing a continuous flow path for itself. As in porous media, the competition for pore occupancy is described by relative permeability and governed by Darcy's law. Darcy's law for single-phase liquid system is:

$$u_l = \frac{k_{abs}(p_i - p_o)}{\mu_l L} \tag{1.1}$$

where subscript $l$ stands for the liquid phase, $i$ for inlet and $o$ for outlet; $\mu$, $p$, $L$, $u$, $k_{abs}$ are the viscosity, pressure, fracture length, Darcy flow velocity and absolute permeability respectively. The Darcy flow velocity is equal to

$$u = \frac{q}{bw} \tag{1.2}$$

with $q$ as the volumetric flow rate, $b$ the fracture aperture and $w$ as the fracture width. Absolute permeability of the fracture is a function only of the fracture aperture (Witherspoon et al., 1980) as described in the relationship:

$$k_{abs} = \frac{b^2}{12} \tag{1.3}$$

For liquid phase in two-phase flow, Eq. 1.1 becomes

$$u_l = \frac{k_{abs}k_{rl}(p_i - p_o)}{\mu_l L} \tag{1.4}$$

where $k_{rl}$ is the relative permeability of the liquid phase.

Similarly, Darcy's law derived for single-phase isothermal gas flow in porous media (Scheidegger, 1974) is:

$$u_g = \frac{k_{abs}(p_i^2 - p_o^2)}{2\mu_g L p_o} \tag{1.5}$$

with the subscript *g* pertaining to the gas phase.

In two-phase flow, Eq. 1.5 becomes

$$u_g = \frac{k_{abs}k_{rg}(p_i^2 - p_o^2)}{2\mu_g L p_o} \tag{1.6}$$

with $k_{rg}$ as the gas relative permeability. The sum of the $k_{rl}$ and $k_{rg}$ indicates the extent of phase interference. A sum of relative permeabilities equal to one means the absence of phase interference. Physically this implies each phase flows in its own path without impeding the flow of the other. The lower is the sum of the relative permeabilities below 1, the greater is the phase interference.

Relative permeability functions are usually taken to be dependent on phase saturation. The two most commonly used expressions for relative permeability for homogeneous porous media are the X-curve and Corey curve (Corey, 1954). The X-curve defines relative permeability as a linear function of saturation:

$$k_{rl} = S_l \tag{1.7}$$

$$k_{rg} = S_g \tag{1.8}$$

where $S_l$ and $S_g$ are the liquid and gas saturation respectively. The Corey curves relate relative permeability to the irreducible or residual liquid and gas saturation, $S_{rl}$ and $S_{rg}$

$$k_{rl} = S^{*4} \tag{1.9}$$

$$k_{rg} = (1-S^*)^2(1-S^{*2}) \tag{1.10}$$

$$S^* = (S_l - S_{rl})/(1-S_{rl}-S_{rg}) \tag{1.11}$$

The equivalent homogeneous single-phase approach treats flow through fracture as a limiting case of flow through pipes. In this model, phase velocities in a fracture are equal and capillary forces are negligible. A continuous flow path is not required for movement of each phase. A phase can be carried along by one phase as bubbles, slug or other complex structures. As in pipes, flow can be described by the concept of friction factors and using averaged properties (Fourar et al., 1993):

$$\frac{(p_i - p_o)}{L} = \frac{\Pi f \rho_m V_m^2}{2A} \tag{1.12}$$

where $\Pi$ is the fracture perimeter, $A$ is the cross sectional area to flow, $\rho_m$ average density and $V_m$ as average flow velocity. The average density is described by:

$$\rho_m = \frac{\rho_g q_g + \rho_l q_l}{q_g + q_l} \tag{1.13}$$

The average flow velocity is equal to:

$$V_m = \frac{q_g + q_l}{A} \tag{1.14}$$

The friction factor, *f*, is derived empirically as a function of the averaged Reynolds number calculated by

$$N_{\mathrm{Re}} = \frac{2bV_m\rho_m}{\mu_m} \tag{1.15}$$

with $\mu_m$ as average viscosity:

$$\mu_m = \frac{\mu_g q_g + \mu_l q_l}{q_g + q_l} \tag{1.16}$$

There are several expressions used to relate friction factor and Reynold's number. The commonly used one for flow through fracture is the generalized Blasius form (Lockhart and Martinelli, 1949):

$$f = \frac{C}{N_{\mathrm{Re}}^n} \tag{1.17}$$

with *C* and *n* as constants derived from experimental data.

According to the results from Diomampo (2001), nitrogen-water flow through fractures is described more appropriately by using the porous medium (relative permeability) approach based on the observations of the multiphase flow behavior. However in the steam-water case, the applicability of the two models for multiphase flow through fractures is still undetermined. From the preliminary results in this research, the steam-water flow shows a different behavior from the nitrogen-water case reported by Diomampo (2001).

## 1.2 LITERATURE REVIEW

The fluids in geothermal reservoirs, steam and water, are both derived from the same substance. However, they form different phases. The phase change during steam-water multiphase flow has made it difficult to investigate steam-water relative permeability. Even in multiphase flow without boiling, only a few published data are available for two-phase flow in fractures. Most of the studies have been done for air-water systems or for water-oil systems.

Earliest is Romm's (1966) experiment with kerosene and water through an artificial parallel-plate fracture lined with strips of polyethylene or waxed paper. Romm found a linear relationship between permeability and saturation, $S_w = k_{rw}$, $S_{nw} = k_{rnw}$ such that $k_{rw}+k_{rnw} = 1$ which represents the X-curve behavior. Fourar et al. (1993) artificially roughened glass plates with beads and flowed an air-water mixture between them. Fourar and Bories (1995) did similar experiments using smooth glass plates and clay bricks. Both studies observed flow structures like bubbles, annular and fingering bubbles comparable to flow in pipes and depicted flow in fractures to be better correlated using the equivalent homogeneous single-phase model. Pan et al. (1996) observed the identical flow structures in their experiments with an oil-water system. They observed that a discontinuous phase can flow as discrete units along with the other phase. Pan et al.

(1996) also found their experimental pressure drop to be better predicted by a homogenous single-phase model. All of these experiments showed significant phase interference at intermediate saturations.

Pruess and Tsang (1990) conducted numerical simulation of flow through rough-walled fractures. They modeled fractures as two-dimensional porous media with apertures varying with position. Their study showed the sum of the relative permeabilities to be less than 1, the residual saturation of the nonwetting phase to be large and phase interference to be greatly dependent on the presence or absence of spatial correlation of aperture in the direction of flow. Persoff et al. (1991) did experiments on gas and water flow through rough-walled fractures using transparent casts of natural fractured rocks. The experiment showed strong phase interference similar to the flow in porous media. The relative permeability data of Persoff (1991) and Persoff and Pruess (1995) for flow through rough-walled fractures were compared in Horne et al (2000) against commonly used relative permeability relations for porous media, the X-curve and Corey curve, as shown in Figure 1.1. Diomampo (2001) performed experiments of nitrogen and water flow through both smooth- and rough-walled artificial fractures, leading to results that are also included in Figure 1.1.

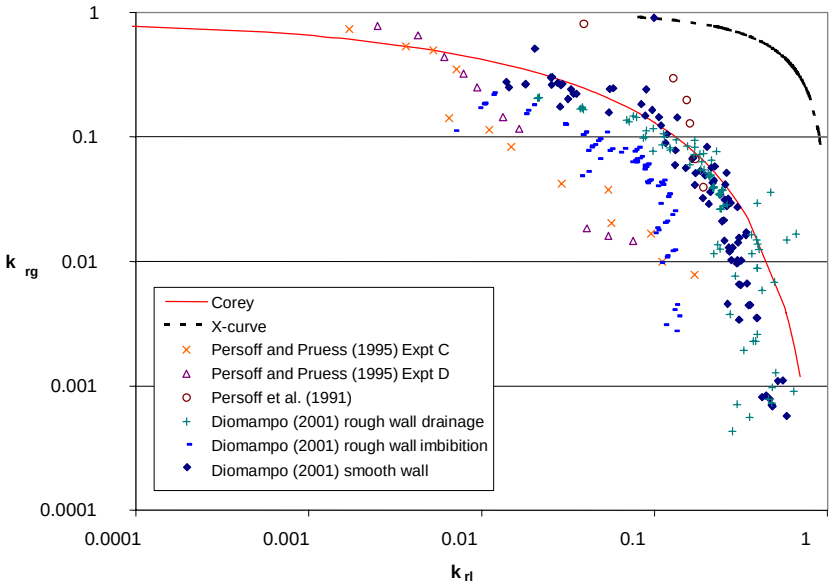


*Figure 1.1: Compendium of previous measurements of air-water relative permeabilities in fractures (from Diomampo, 2001).*

In the experiments of both Persoff (1991) and Persoff and Pruess (1995), flow of a phase was characterized by having a localized continuous flow path that is undergoing blocking and unblocking by the other phase. Recent parallel plate experiments by Su et al. (1999) illustrate the same flow mechanism of intermittent localized fluid flow. Kneafsy and Pruess (1998) observed similar intermittent flow in their experiments with pentane through various parallel plate models made from glass, sandblasted glass or transparent fracture replicas. Diomampo (2001) also observed the intermittent phenomenon in her

experiments. Furthermore, the results from Diomampo (2001) conform mostly to the Corey type of relative permeability curve (Figure 1.1). This suggests that flow through fractures can be analyzed by treating it as a limiting case of porous media flow and by using the relative permeability approach. These observations are contrary to the findings of Fourar et al (1993), Fourar and Bories (1995), and Pan et al. (1996).

Presently, the mechanism of flow and the characteristic behavior of relative permeability in fractures are still not well determined. Issues such as whether a discontinuous phase can travel as discrete units carried along by another phase or will be trapped as residual saturation as in porous medium are unresolved. The question of phase interference i.e. is the relative permeability curve against saturation an X-curve, Corey or some other function, is still unanswered. The main objective of this study is to contribute to the resolution of these issues. Experiments on flow through smooth-walled fractures without boiling have been conducted by Diomampo (2001), who established a reliable methodology for flow characterization and permeability calculation for nitrogen-water flow. Currently, steam-water system experiments are in progress.

## 1.3 EXPERIMENTAL METHODOLOGY

The steam-water flow experiment is more complex the than air-water experiment conducted previously by Diomampo (2001). The steam-water flow experiment has to be performed at high temperature. The whole experiment system is illustrated in Figure 1.2, which shows the deaerated water supply, the fracture apparatus (inside the air bath), data acquisition system, and digital image recording (also see Figure 1.9).

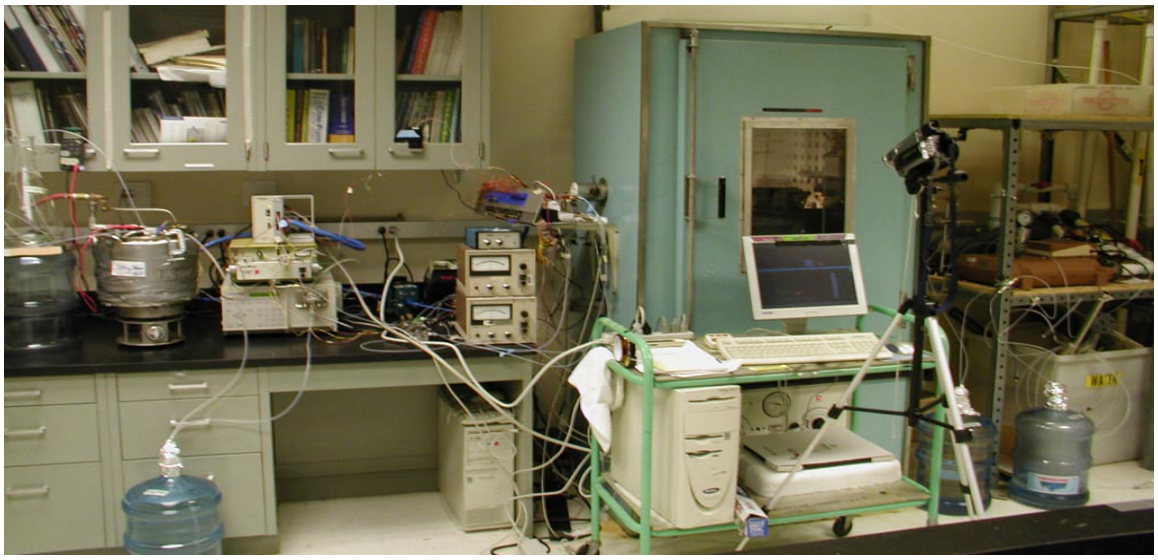

*Figure 1.2: Picture of steam-water flow through fracture apparatus.*

### Fracture Apparatus Description

The fracture is created by a smooth glass plate on top of an aluminum plate, confined by a metal frame bolted to the bottom plate. The frame was designed to improve the seal and to prevent deformation of the glass due to system pressure. The metal frame has

several windows and a mirror attached to it for flow visualization (see Figure 1.3 and Figure 1.4.)

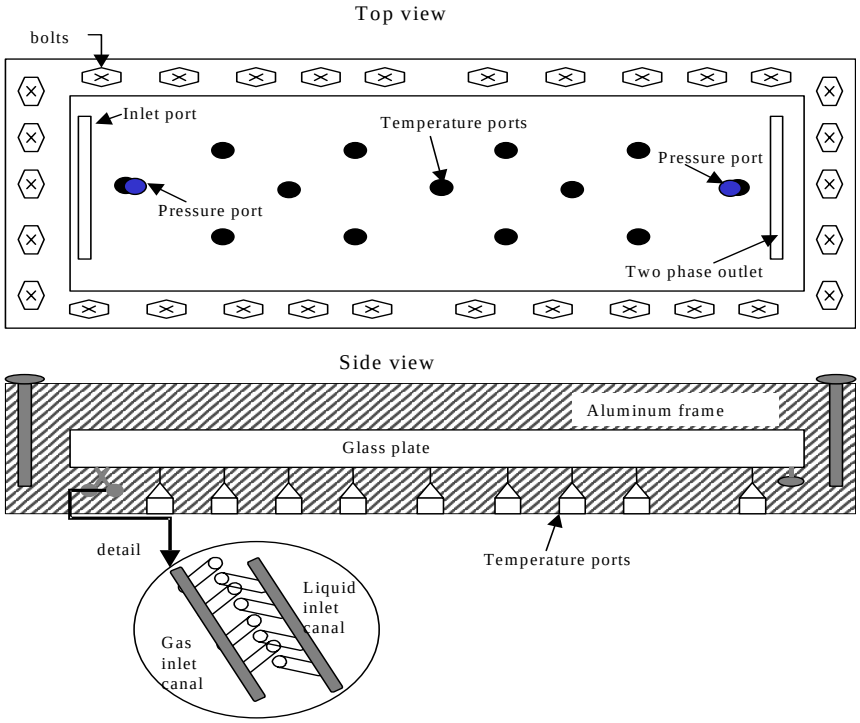


*Figure 1.3: Schematic diagram of fracture apparatus.*

*Figure 1.4: Picture of fracture apparatus.*

An O-ring (Viton 1/8" thick #2-272) was placed in between the glass and aluminum plate as a seal (see orange color lining in Figure 1.4). Placing this O-ring in the channel was not sufficient to provide a good seal because the channel was custom made in width and length. Thinly cut rubber sheets were placed at the outer boundary to push the O-ring to the sides of the aluminum plate. These provided an excellent seal when compressed with the glass and metal frame. Since the O-ring is cylindrical in shape and the aluminum

plate is rectangular, there is a narrow channel in between the O-ring and the plate when squeezed together. A thin lining of copper-based adhesive (Permatex Ultra Copper) was applied to fill this channel. It is important to eliminate this channel for it serves as an easy conduit for the fluid to pass through instead of the fracture.

The phases enter the fracture through two separate canals. Each canal has several ports drilled in a way that they align on the surface (see Figure 1.3). In the nitrogen-water experiments both entry canals were used, but in the steam-water experiments only water was injected and the steam was created by boiling within the fracture itself. The surface of the fracture apparatus was designed such that there is an available 12 inch by 4 inch space for flow. Throughout this flow area, tiny temperature ports the size of needles were drilled. Needle-size ports were drilled so as to minimize surface discontinuity. A pressure port was drilled at each end of the flow path. The two-phase fluid exits through a single outlet.

**Fractional Flow Ratio Detector (FFRD)**

One of the biggest challenges of the steam-water flow experiment is to measure the steam and water flow rates, since there is phase transition occurring when steam and water flow through the fracture. Therefore using flow meters to measure the rate of each phase becomes inappropriate, because it is always impossible to separate steam from water without any mass loss or gain. To overcome this situation, an in-situ fractional flow ratio detector (FFRD) was designed and constructed as shown in Figure 1.5. The principal of the FFRD is that different phases will have different refractive indices. A phototransistor (NTE 3038, NPN-Si, Visible, Vcbo 25V, Ic 20mA, Pd 50 mW, response time 1.5 μs) was installed inside the FFRD, producing different voltages when sensing different strengths of light. The water phase produces a higher voltage when flowing through the FFRD. In order to minimize the heat loss between the outlet of the fracture apparatus and the FFRD, the FFRD device was installed as close to the outlet of the fracture as possible (about 5cm distance). An example of the FFRD response signal during testing is shown in Figure 1.6.

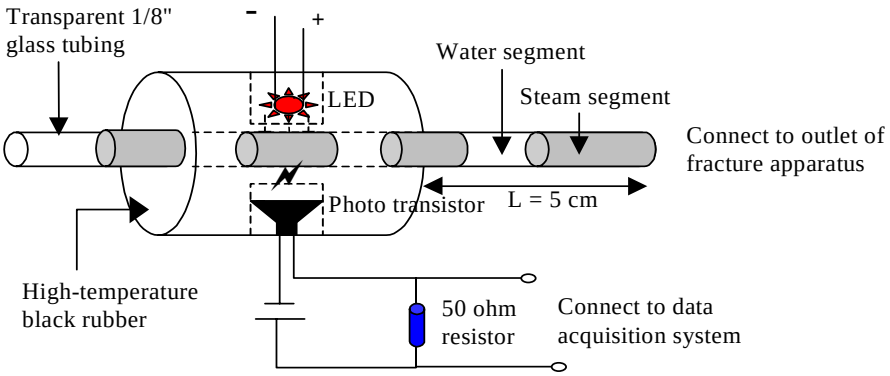


*Figure 1.5: Schematic of fractional flow ratio detector (FFRD).*

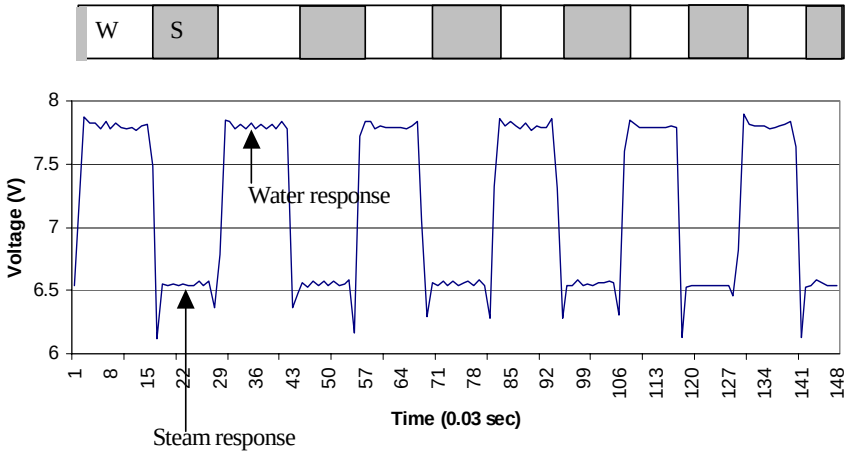


*Figure 1.6: The signal of steam and water detected from fractional flow ratio detector.*

Once the steam and water responses are obtained from the FFRD, the statistical histogram is plotted and the steam and water phase flow ratios are obtained by determining the threshold of the histogram. This is shown in Figure 1.7 and Table 1.1.

The calibration test of FFRD has been completed as shown in Figure 1.8. As can be seen from Figure 1.8, at both high and low water flow rates the FFRD shows high accuracy in measuring fractional flow at different nitrogen flow rates. Even when the nitrogen flow rate is much higher than the water flow rate, the FFRD can recognize the fractional flow ratio over a period of several seconds. Therefore, the FFRD technology should be appropriate to calculate steam and water outlet flow rates.

*Table 1.1: The analysis results of steam and water fractional flow ratios from Figure 1.7.*

| *Bin* | *Frequency* | Discrimination |
|---|---|---|
| 6.2 | 287 | Steam |
| 6.4 | 603 | Steam |
| 6.6 | 7021 | Steam |
| 6.8 | 600 | Steam |
| 7 | 110 | Steam |
| 7.2 | 20 | Threshold |
| 7.4 | 146 | Water |
| 7.6 | 400 | Water |
| 7.8 | 3810 | Water |
| 8 | 3462 | Water |
| More | 0 | |

| | |
|---|---|
| Steam Total | 8631 |
| Water Total | 7828 |
| Grand total | 16459 |

| Fractional flow | |
|---|---|
| Steam | 0.5243939 |
| Water | 0.4756061 |

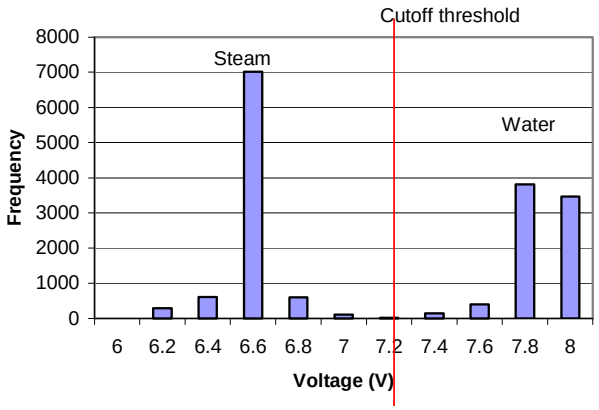


*Figure 1.7: The histogram obtained from Figure 1.6.*

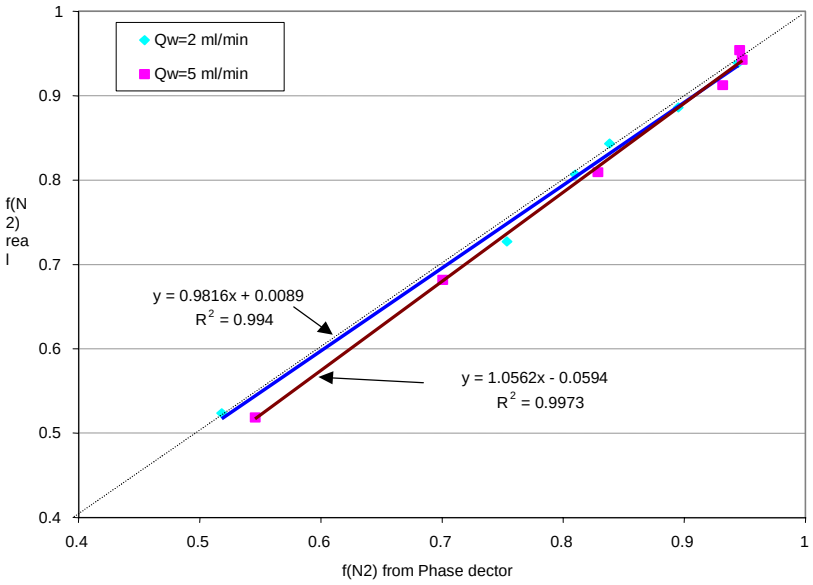


*Figure 1.8: The calibration of FFRD in nitrogen-water flow.*

## 1.4 CONTROL AND MEASUREMENT TECHNIQUES

There are two methods available to produce steam-water flow inside the fracture. One method is by injecting steam and water separately into the apparatus. The steam would be produced using a steam generator inside the air bath to boil steam from deaerated water. The other method is by injecting only deaerated water into the apparatus, after which the steam phase is produced by adjusting either pressure or temperature in the fracture. Since the steam quality from the steam generator is hard to control, the heat loss from the steam generator to the fracture apparatus is hard to determine, and there is a significant phase transformation at the moment when the injected steam and water meet in the inlet port, the latter method was used in this experiment.

The two factors that control the steam production are temperature and pressure. According to experience, adjusting pressure requires less equilibration time than adjusting temperature. To facilitate pressure adjustment, a physical back-pressure device was connected to the outlet of the apparatus to constrain the pressure inside the fracture to a specific. For water, a meter pump (Dynamax, SD-200) controlled the rate of injection. The water used in the experiment needs to be deaerated almost completely. To reach this quality, distilled water was evacuated using a vacuum pump for 2 hours, and then the water was boiled to achieve a low dissolved-gas condition. This distilled, deaerated water was used as the injection fluid. Figure 1.9 shows a schematic diagram of this configuration.

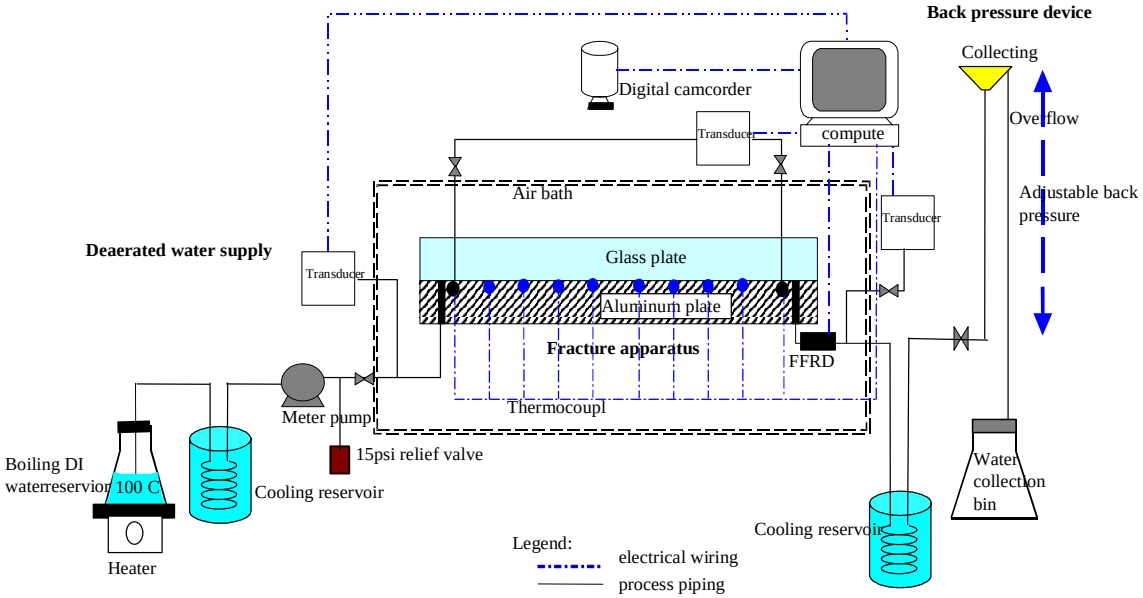


*Figure 1.9: Process flow diagram for steam-water experiment.*

## Pressure

Low-range differential transducers were used to measure the pressure drop through the fracture, as well as the water inlet pressure and the two-phase outlet pressure. The liquid differential transducer (Celesco Transducer Model CD 10D range 0-5psi) was attached to both pressure ports inside the fracture to measure the pressure drop through the fracture. Another transducer (Celesco Transducer Model CD 10D range 0-25psi) was attached to the water inlet. The third transducer (Celesco Transducer Model CD 10D range 0-25psi) was attached to the two-phase outlet of the fracture apparatus. These transducers send electrical signals to the SCXI-1000 data acquisition device, which was monitored using the LabView® programmable virtual instrument software.

## Flow rates, $q_w$ and $q_s$

For steam and water flow rates measurement, the fractional flow ratio detector (FFRD) was used to measure the outlet steam and water fractional flow ratio, $f_s$ and $f_w$.

$$f_s = \frac{q_{out,s}}{q_{out,t}} \tag{1.18}$$

$$f_w = \frac{q_{out,w}}{q_{out,t}} \tag{1.19}$$

where $q_{out,s}$ is the output steam flow rate, $q_{out,w}$ is the output water flow rate, and $q_{out,t}$ is the output total flow rate. Once $f_s$ and $f_w$ are obtained, it is easy to evaluate $q_{out,s}$ and $q_{out,w}$ by using mass balance if a steady-state condition is reached. In order to catch the fast and unsteady steam and water segment in the outlet tubing, The FFRD was connected to the SCXI-1000 data acquisition device, which has 50Hz maximum sampling frequency.

Once fractional flows are known, the steam and water flow rate can be calculated according to the mass balance under the assumption of steady state. The mass balance equation is:

$$m_{in} = q_{in,t}\rho_{w,at104^o c} = m_{out} = m_{out,w} + m_{out,s} = q_{out,t}(f_w\rho_{w,at104^o c} + f_s\rho_{s,at104^o c}) \tag{1.20}$$

where, $m_{in}$, $m_{out}$ stand for the input and output mass, $q_{in,t}$ and $q_{out,t}$ stand for input and output volumetric flow rates, $\rho$ is the density, and $f_s$ and $f_w$ are steam and water fractional flows.

If $f_s$ and $f_w$ are known from FFRD data, the total output flow rate, $q_{out,t}$, can be obtained from Eq. 1.20:

$$q_{out,t} = \frac{m_{in}}{f_w\rho_w + f_s\rho_s} \tag{1.21}$$

The end-point steam and water flow rates are:

$$q_{out,w} = f_w q_{out,t} = f_w \frac{m_{in}}{f_w\rho_w + f_s\rho_s} \tag{1.22}$$

$$q_{out,s} = f_s q_{out,t} = f_s \frac{m_{in}}{f_w\rho_w + f_s\rho_s} \tag{1.23}$$

Since the flow rates obtained are end-point flow rates, they can represent true flow rates under steady-state conditions. If the flow is in an extremely unsteady state, some mixed phase response will happen in the FFRD, and the flow rates calculated will become incorrect. However, if the flow is in quasisteady state, for example, the steam or water flow rate increases at a fairly slow rate, flow rates obtained by this method should approximate the real flow rates except for a short delay of the phase response.

**Saturation**

Still images were taken from the recorded video. The data gathered from the video were correlated with the Labview data through the time read from the LCD monitor. Figure 1.10 shows a typical video image taken from the experiments. From the still image shown in Figure 1.10, saturation was computed by measuring the area that each phase occupied. The photographs were processed in a Matlab® program. The program first cuts the photograph to display just the image of the flow area. Using this cut image, the program

does quadratic discriminant analysis (QDA) to group the pixels of the picture into three groups: the water phase, steam phase and the frame. The grouping is based on color differences. Saturation is calculated as total pixels of the liquid group over the sum of the steam and liquid groups. Figure 1.11 is a comparison of the gray-scaled image produced by the QDA program and the original cut photograph from the digital camcorder. The accuracy of the program in calculating the saturation can be related to the similarity in details of the gray scale image to the true image. From the figure, it can be said that the program has reasonable accuracy.

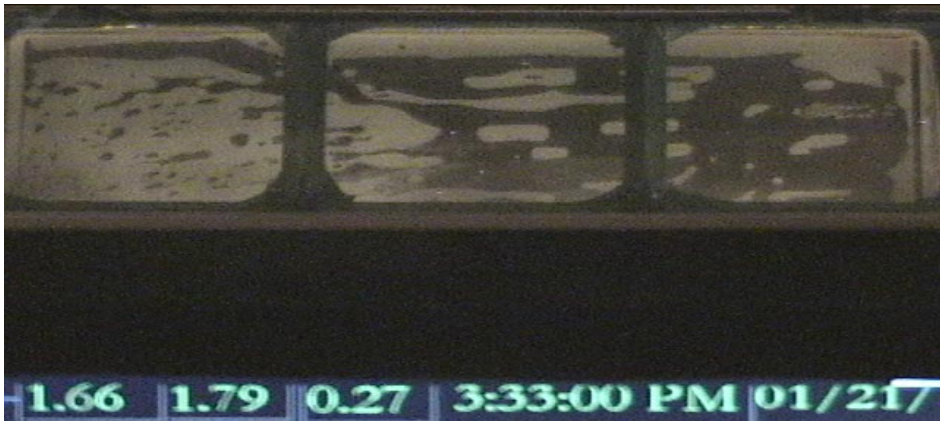


*Figure 1.10: Sample video image taken for steam-water runs.*

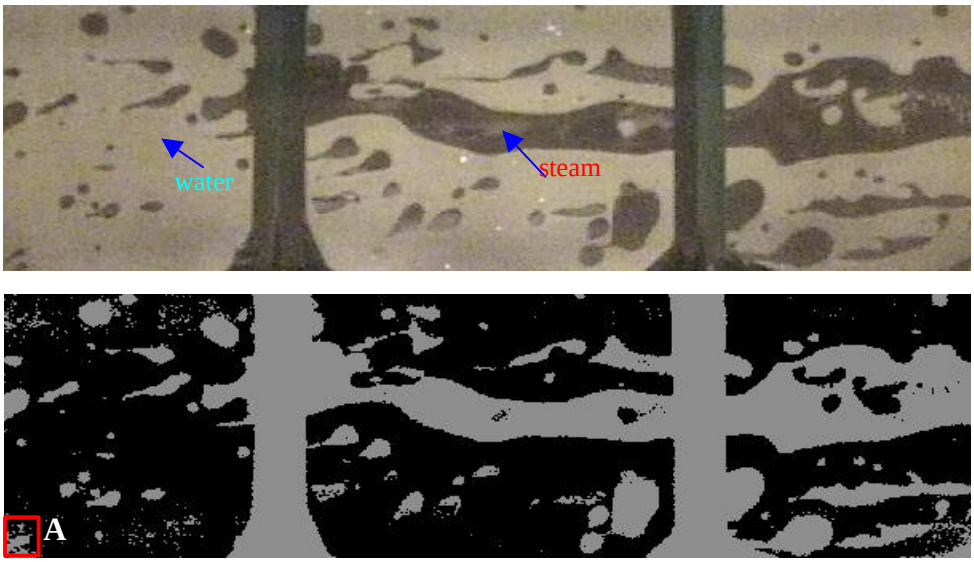


*Figure 1.11: Comparison between the true color image of the fracture flow and gray scale image from Matlab QDA program used in measuring saturation.*

Pan et al. (1996) also used this technique for measurement of saturation. This study noted that the sources of error in this technique were the quality of the photographs and the water film adsorbed on the surfaces of the plates with the latter being of minimal

effect. Good quality photographs are the ones with clear distinction between the gas and liquid phase. Good lighting is necessary so that the colors in the image come out clearly. The lighting should also be positioned in a way that it does not produce shadow on the flow area. The program will mistakenly take the shadow as steam phase even if there is liquid (Zone A in Figure 1.11).

According to the nitrogen-water experiments by Diomampo (2001) and others, these fracture flow experiments are not expected to reach a perfect steady state. Instead, they are unsteady by nature. There are significant pressure fluctuations accompanied by saturation changes and the gas and water flow rates vary. Due to this behavior, the data acquisition task requires frequent gathering of instantaneous pressure, flow rate and saturation values. Instantaneous gathering of data was accomplished by the use of a digital video camcorder. Video shots were taken of the pressure, time and saturation data displayed all at the same time. Pressure and temperature data and related time were displayed by the LCD monitor connected to the computer, which also ran the data acquisition system. The saturation was computed from the image of the whole flow area of the fracture. The methodology used to integrate all the data and signal and then calculate the steam-water relative permeabilities can be explained simply by the flow chart in Figure 1.12.

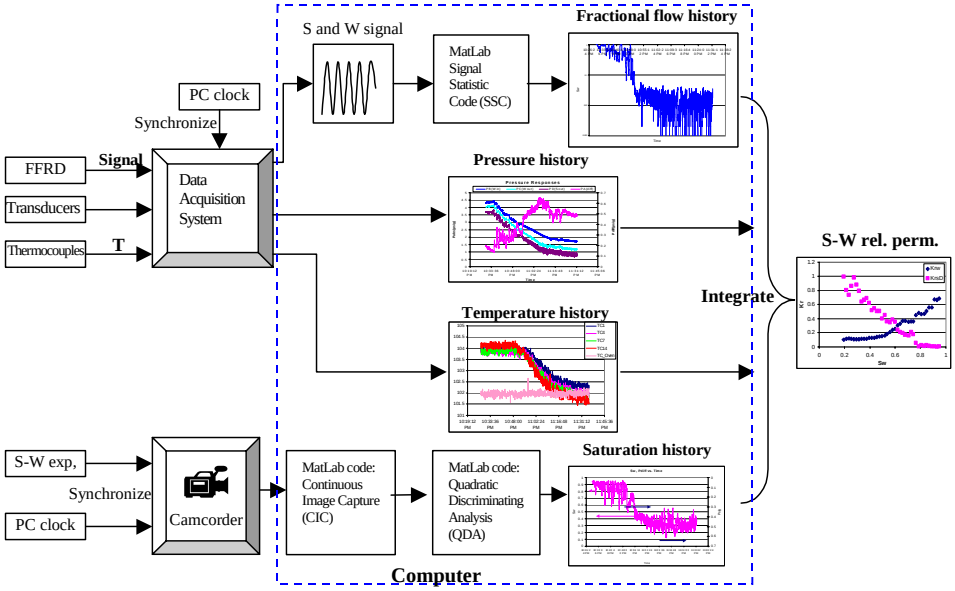


*Figure 1.12: data and signal processing flowchart.*

## 1.5 PRELIMINARY RESULTS AND DISCUSSION

### Absolute Permeability of the Fracture

The absolute permeability of the fracture under water flow was measured at high temperature (~95°C) with different back pressures. High temperature makes the system close to the relative permeability experiment condition. Having different back pressures

allows us to examine whether the back pressure is strong enough to alter the fracture aperture. If such an alteration happens, the subsequent experiments will be subject to the permeability correction according to their back pressure.

Figure 1.13 shows the absolute permeability of the fracture in deaerated deionized water flow under a 95 $^{o}$C environment. According to Figure 1.13, the permeability is close to constant (~1020 darcy) except for one outlier at 1265 darcy when the back pressure is less then 4psig. An increasing permeability trend can be seen when the back pressure is greater than 4 psig, which means the top glass of the fracture may be lifted by high pressure or this may be due simply to measurement error. Fortunately, subsequent experiments will be just going to 4 psig maximum pressure. Therefore, the average permeability (1020 darcy) taken from 0 to 3 psig was adopted for the relative permeability calculation.

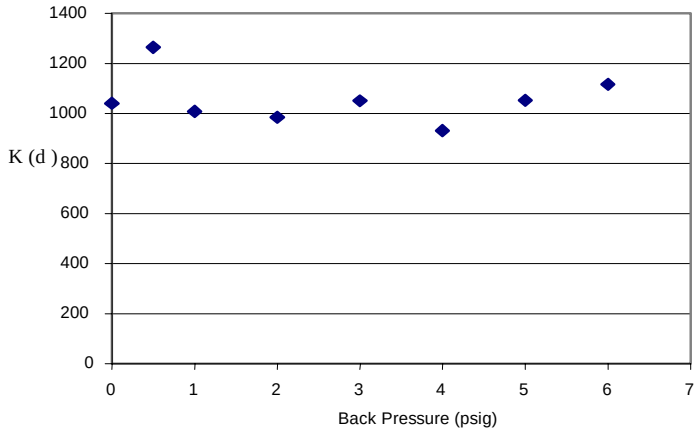


*Figure 1.13: Absolute permeability in different back pressure at 95$^{o}$C*

## Steam- and Nitrogen-Water Flow Behaviors

A drainage steam-water flow through a smooth-walled fracture experiment has been conducted. Some images have been analyzed, and the corresponding saturation has been obtained satisfactorily. As observed from the video record, the steam-water flow behavior in the fracture is significantly different from the nitrogen-water flow behavior described by Diomampo (2001) in the same fracture.

Figure 1.14 shows four consecutive images (under high water saturation) taken when the water injection rate was 2 ml/min, temperature is 102$^{o}$C, and pressure was around 16.5 psia. The steam (dark part) never forms a stable path or channel, but behaves like moving fingers, slugs and bubbles. These physical phenomena are different from those observed in nitrogen-water flow by Diomampo (2001) as shown in Figure 1.15.

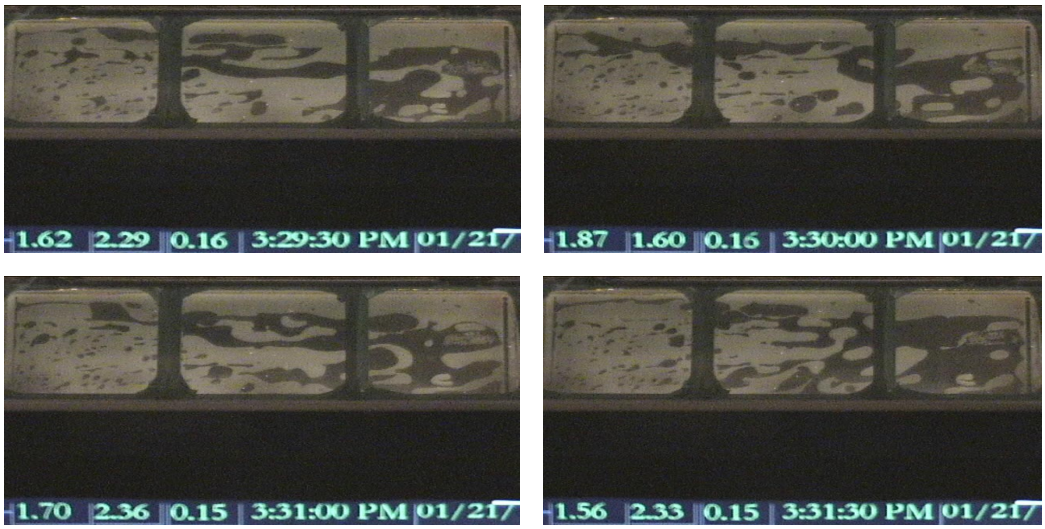


*Figure 1.14: The continuous steam-water flow behavior in smooth-walled fracture under high water saturation (>65%). (steam phase is dark, water phase is light).*

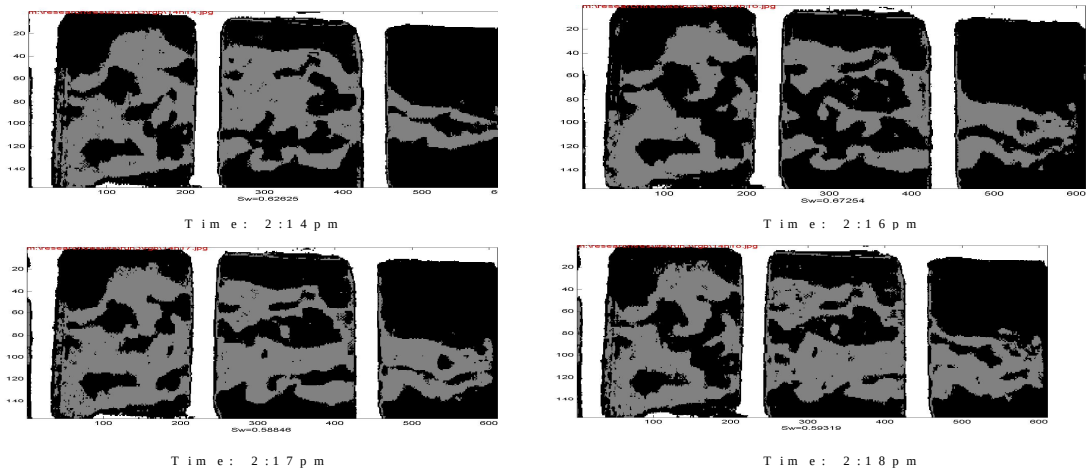


*Figure 1.15: The continuous nitrogen-water flow behavior in smooth-walled fracture. Images showing the forming and breaking of gas flow path (light part) (images from Diomampo, 2001).*

Comparing Figure 1.14 to Figure 1.15, there is less steam phase near the inlet (the left side) in the steam-water flow in comparison to the nitrogen phase near the inlet in nitrogen-water flow. This is because the phase transformation from water to steam as pressure decreases in the steam-water flow. Hence the farther the water flows, the more steam it produces. This will be an important factor affecting the steam-water flow behavior under high water saturation situations (>65%). Figure 1.16 shows the steam-water flow under low water saturation (<15%). In this case, it is water that behaves like moving fingers, slugs (the red circle in Fig. 1.16) and bubbles. These physical phenomena are different from those observed by Diomampo (2001) in nitrogen-water flow. According to these preliminary findings, the steam-water flow in fractures might be more suitably described by the equivalent homogeneous single-phase approach.

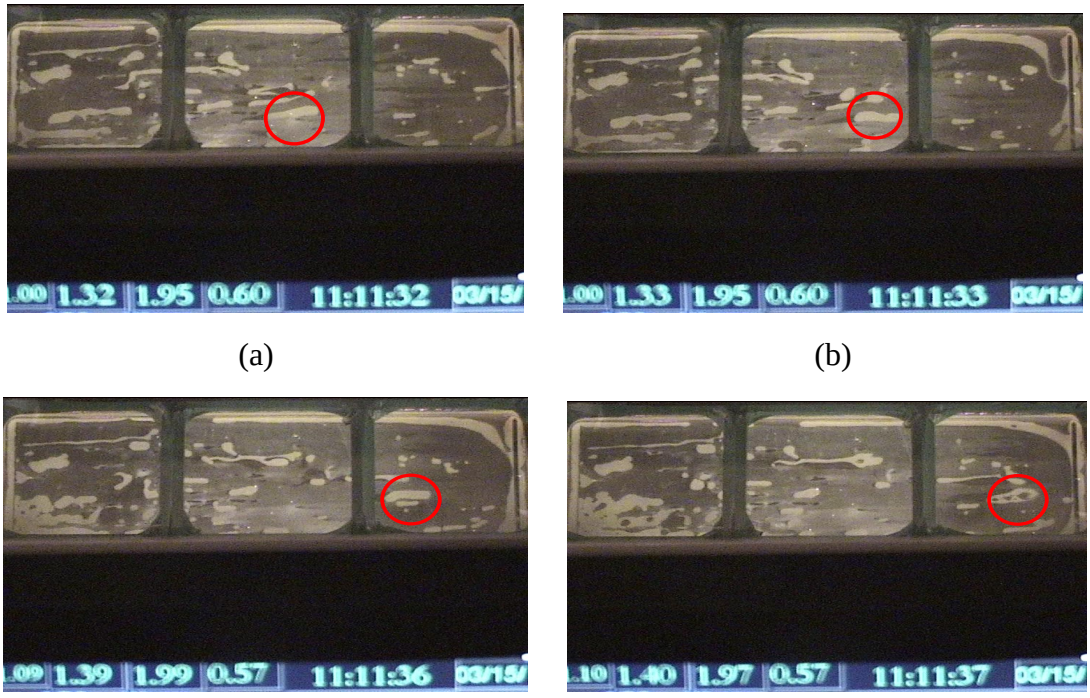


(a) (b)

(c) (d)

*Figure 1.16: The continuous steam-water flow behavior in smooth-walled fracture under low water saturation (<15%). (steam phase is dark, water phase is light).*

## Unsteady Steam-Water Relative Permeability Experiment

An unsteady steam-water relative permeability experiment was conducted. In this experiment, the back pressure device in Figure 1.9 was modified to allow the pressure to decrease at a constant rate automatically. To accomplish this goal, a low RPM gearhead motor (2-6 RPM) and a pulley set was installed to control the back pressure. The detail of the back pressure device in the unsteady state experiment is shown in Figure 1.17.

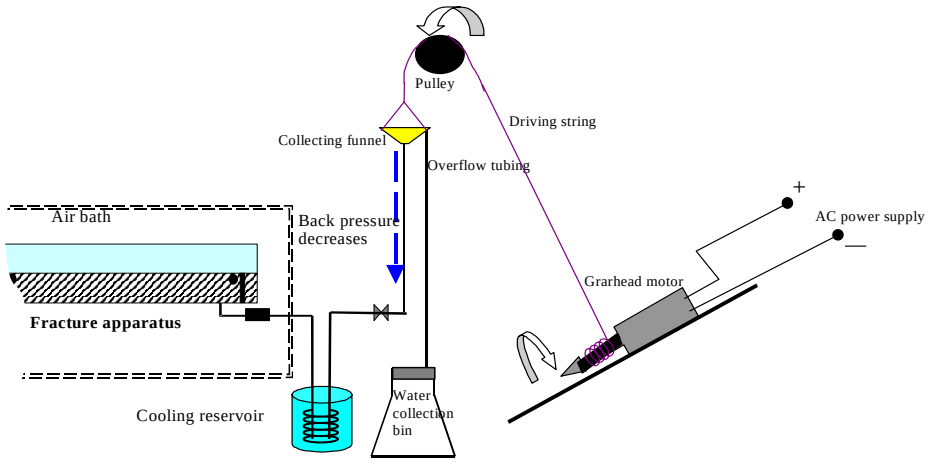


*Figure 1.17: Schematic of back pressure control in unsteady state experiment.*

The rotation rate of the gearhead motor was set to 3 RPM such that the rate of pressure decrease reaches 0.1psi/min. The starting back pressure was 3.3 psig. While the back

pressure was decreasing continuously, the saturation images, pressure from each transducer, temperature from each thermocouple and fractional flow were recorded to the digital camcorder and to the computer via data acquisition system.

In the unsteady experiment, the back pressure was decreased continuously from 3.3 psig to 0 psig in 30 minutes. The experiment was recorded for this duration and for another 30 more minutes after zero back pressure was reached, using the digital camcorder. This one-hour video was then captured and transformed to still JPEG images in one-second periods by the MatLab CIC program. Therefore around 3600 images were obtained. These images were then subject to the Quadratic Discriminating Analysis (QDA) program to perform water saturation calculation. Figure 1.18 shows the input, output and differential pressure responses during the experiment. The analysis result is shown in Figure 1.19. As can be seen in Figure 1.19(a), the change of the water saturation is consistent with that of pressure difference (inverted axis) along the fracture. Figure 1.19(b) also shows high correlation between the water saturation and pressure difference. This is consistent with the physical explanation. When the back pressure decreases at a boiling temperature, the steam quality increases, which means steam saturation and volumetric flow rare increase. Since the increase of steam flow rate is much higher than the decrease of water flow rate according to mass balance, the pressure drop also increases. The saturation and pressure fluctuations in Figure 1.17(a) are due to the unsteady nature of the flow.

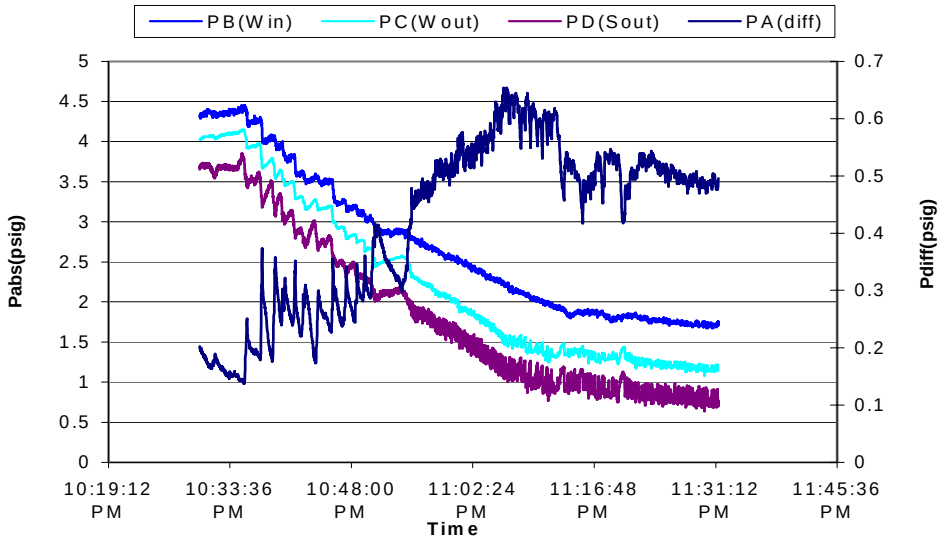


*Figure 1.18: Pressure responses during unsteady experiment.*

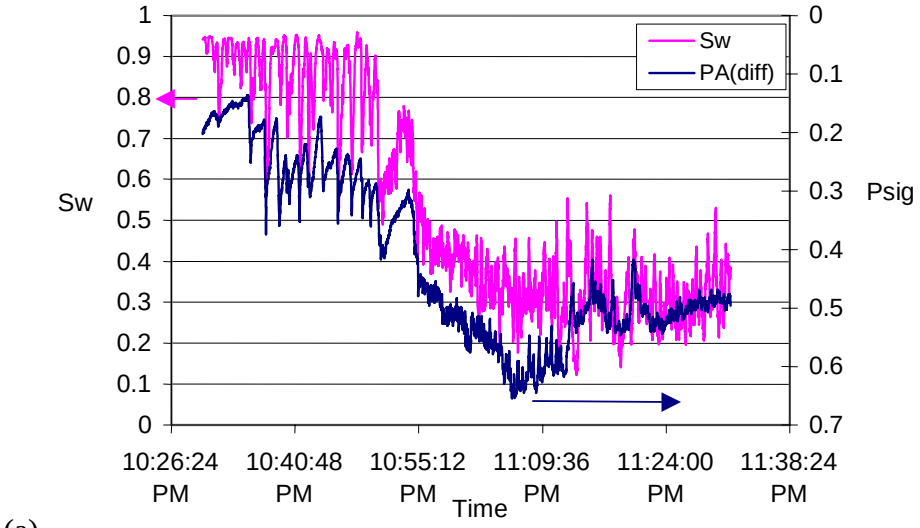


(a)

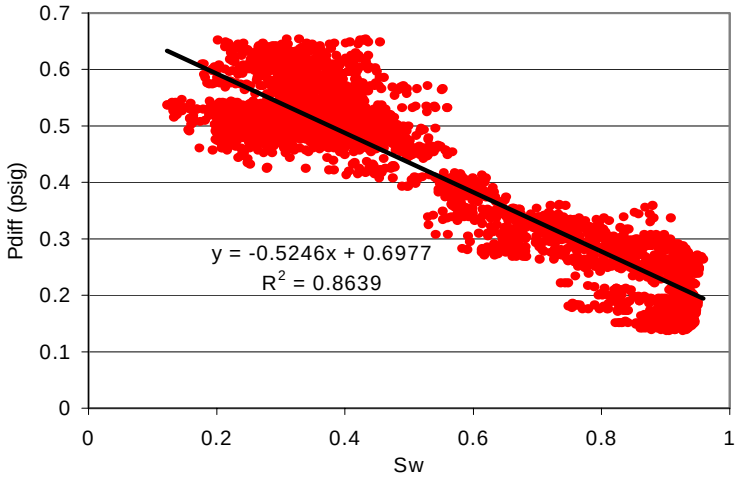


(b)

*Figure 1.19: Water saturation versus pressure difference in unsteady experiment.*

The signal of steam and water response from the FFRD was sent to the MatLab Signal Statistical Code (SSC) to perform the fractional flow calculation. Figure 1.20(a) presents the result of the water fractional flow response and saturation versus time. The y-axis of $f_w$ is logarithmic whereas that of $S_w$ is linear. Again, the trend of water fractional flow is consistent with that of water saturation. However, some offset of $f_w$ and some mismatch of amplitudes in these two curves was found (Figure 1.20(b)). This may be due to both measurement error and computer analysis error. The offset of the $f_w$ curve results mainly from the delay of the saturation response from the fracture to the FFRD at the outlet of the aparatus and the smoothing effect due to the discretized period, i.e. the period used to calculate one point of $f_w$. These errors would play an important role in the relative permeability calculation.

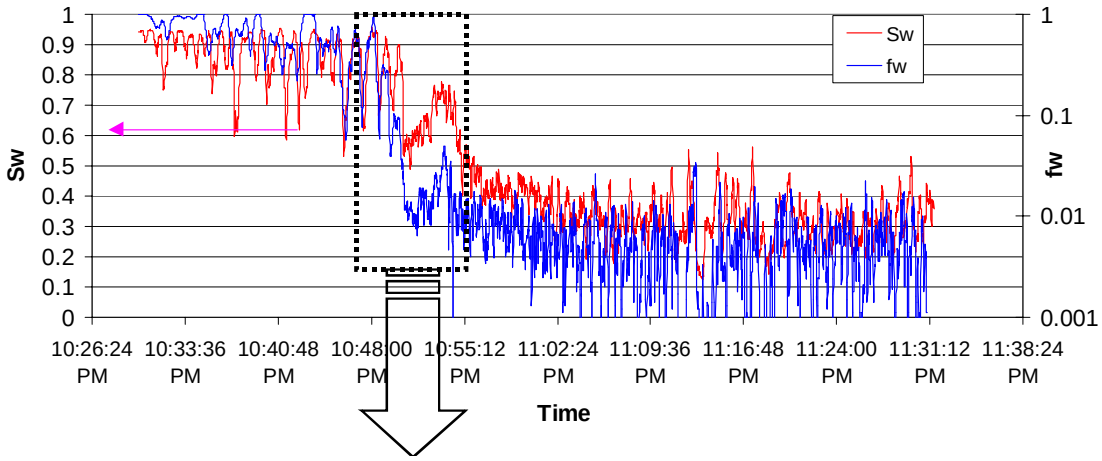


(a)

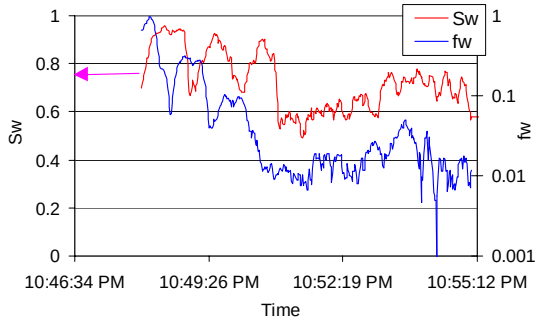


(b)

*Figure 1.20: Water fractional flow ($f_w$) and saturation ($S_w$) versus time in the unsteady experiment.*

The temperature distributions as functions of position and time are shown in Figure 1.21 and 1.22 respectively. From Figure 1.21, the temperature change from upstream to downstream in the fracture is within 0.5$^o$C. However, a near 2$^o$C temperature difference between the fracture and air bath in the initial single-phase (water) flow can be seen in Figure 1.22. This results from the warm-up effect caused by the lighting system installed at the back of the fracture apparatus. When steam quality increases, due to the high velocity and lower conductivity of steam, the apparatus temperature will approach the environmental (air bath) temperature gradually as shown in Figure 1.22. This situation might affect the experimental result if the energy balance and heat loss calculations are applied, since the condition is not adiabatic. However, the effect may be limited if the steam and water flow rates are obtained from the FFRD directly.

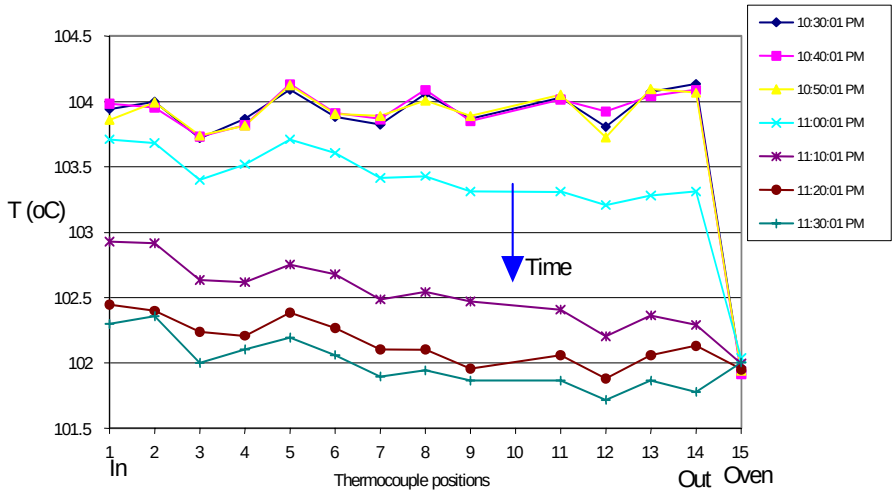


*Figure 1.21: Temperature distribution through the fractures in steam-water unsteady experiment.*

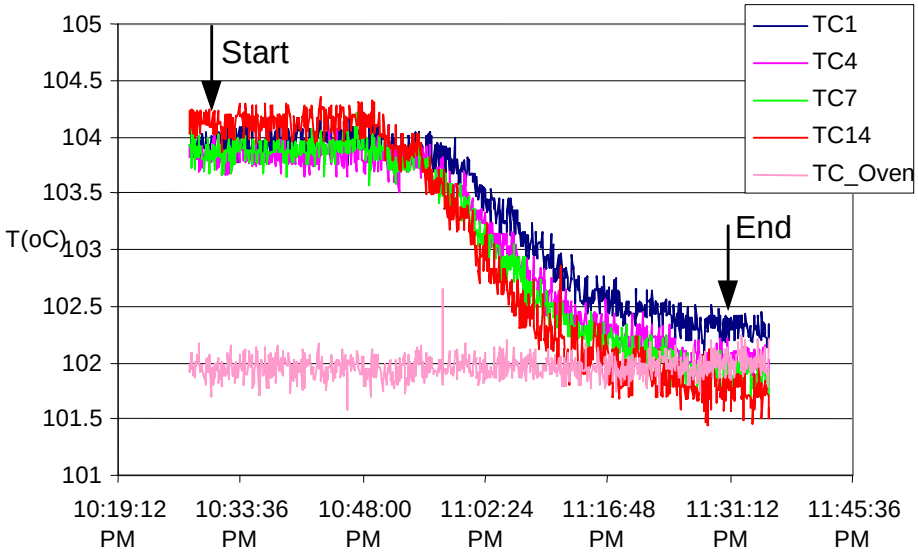


*Figure 1.22: Temperature history in steam-water unsteady experiment.*

After combining the pressure, temperature, saturation, fractional flow information in Figures 1.19, 1.20, and 1.21, the steam-water relative permeabilities can be calculated by using Eqs. 1.14, 1.16, 1.22 and 1.23. Figure 1.23 is the calculation result of 2670 data points out of a total of 3660 points. The remaining 990 points were either negative or unphysical (for example $k_r$>>1) due to measurement error or noise. The $k_{rw}$ curve behaves smoothly, whereas the $k_{rs}$ curve is more scattered. As mentioned before, this scattered effect may be associate with the steam and water flow rate measurement error. The detail of this error is due to the delay of $f_s$ and $f_w$ measurement from the FFRD and the measurement error caused by extremely high-speed steam flow which collapses the water component into many tiny water drops that are hard to detect in the image analysis. This will lower the measurement accuracy significantly.

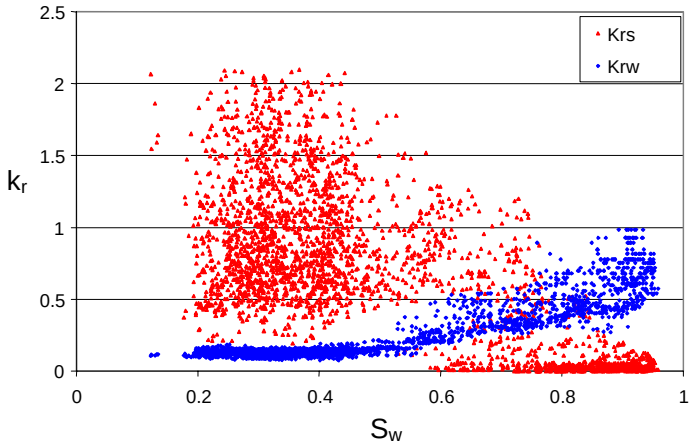


*Figure 1.23: Steam-water relative permeability in the unsteady experiment.*

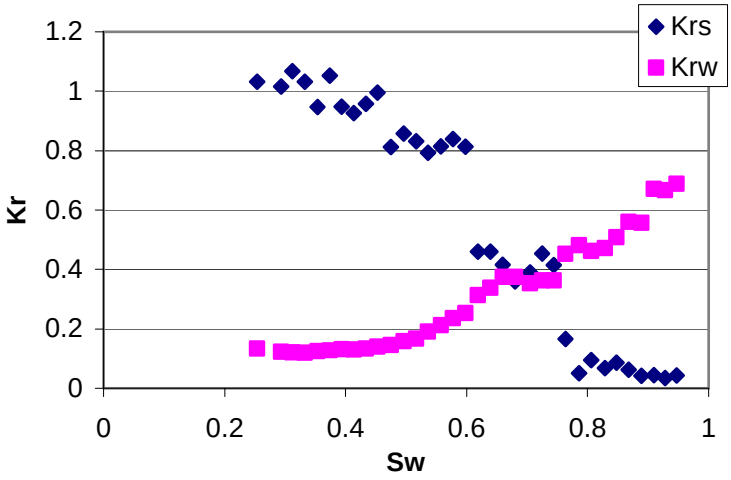


*Figure 1.24: Steam-water relative permeabilities in the unsteady experiment by using 2% $S_w$ averages.*

Further processing was applied to Figure 1.23 to characterize the steam-water flow behavior. Figure 1.24 was obtained by averaging the relative permeability over 2% saturation ranges from Figure 1.23. The figure shows the fracture medium to be water wet since the two curves cross at near 70% water saturation. This is as expected because the aluminum and glass materials both have water-wet properties. What is interesting is that the sum of these two curves is close to 1 which indicates less phase interference. This result is different from the nitrogen-water relative permeabilities which showed a near Corey-type relative permeability behavior. Figure 1.25 shows the comparison of steam-water and nitrogen-water relative permeability curves. The nitrogen-water experiment was conducted by Diomampo (2001) who used the same fracture apparatus but at room temperature. The liquid curves have almost identical trends except in low water saturation range where the steam-water case may lose some accuracy because of the error from the FFRD. On the other hand, the gas curves behave very differently. The steam curve shows a much more mobile character than the nitrogen curve, which can be

seen from the higher relative permeability values in the steam curve. This phenomenon was also observed from the digital images.

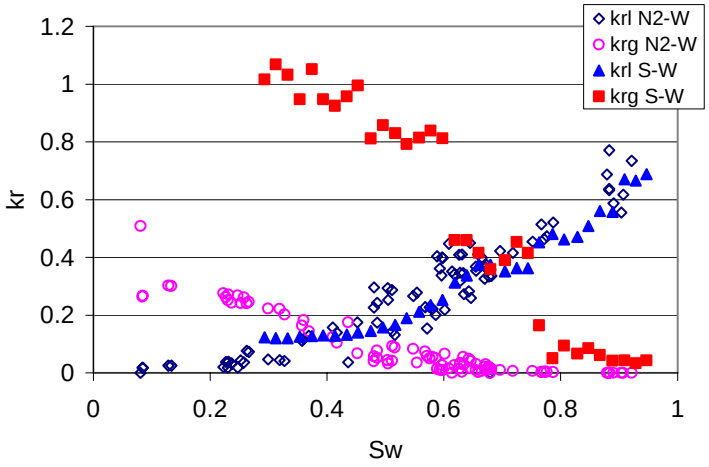


*Figure 1.25: Comparison of relative permeability curves between steam- and nitrogen-water cases in the smooth wall fracture.*

Figure 1.26 compares this result with previous research into air-water relative permeability in fractures. Most of these studies proposed that the air-water relative permeabilities in fractures follow Corey-type curves. However, as can be seen in Figure 1.26, the steam-water relative permeabilities behave closer to the X-curve.

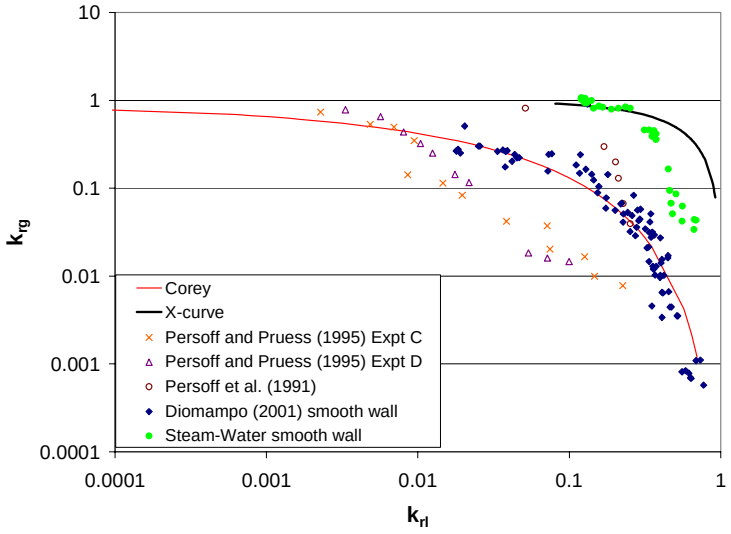


*Figure 1.26: Comparison of steam-water relative permeability with previous measurements of air-water relative permeabilities in fractures.*

Using the equivalent homogeneous single-phase approach to model steam-water flow in fracture is under investigation. Also the correction of gas-slippage effect has not yet been applied.

**Sources of Error**

End effect: As can be seen in Figure 1.6(c) and (d), there exist end effects near the inlet and outlet of the fracture. These will lead to overestimation of the water saturation. To overcome this problem, the very left and right parts of the image should be cut. Hence, the pressure measurement should be modified. Either drilling new pressure ports at inner positions or using a method to infer the pressure from the saturation temperature should be utilized.

Pressure oscillation: This resulted from boiling inside the pressure tubing. The boiling produces steam phase inside the pressure tubing in which only water phase is expected to exist. Unfortunately, this two-phase coexistence is unsteady. The evaporation and condensation rate depend highly on the system pressure and temperature.

Saturation calculation error: The quadratic discriminant analysis program will lose accuracy if there is some fog or cloudiness on the surface of the top glass of the fracture. This will overestimate the water saturation.

Flow rate measurement error: During steam-dominated flow, the liquid segments inside the FFRD will collapse and form small water drops as described in the previous section. Further nitrogen-water corrections will be developed at extremely high air flow rate to address this problem.

Heat gain and loss: The illumination bulbs seem to heat the fracture apparatus. The temperature loss through the fracture is less than $0.5^{o}$C. These effects are still under investigation.

## 1.6 FUTURE WORK

The purpose in conducting the unsteady experiment first is that allows us not only to measure the relative permeability, but also to observe the transients of steam-water flow. Nevertheless, the unsteady experiments are also more uncertain. The steam phase relative permeability curve in the unsteady experiment is very scattered. This might be attributed to measurement error, or this may be the nature of steam-water flow in fractures, which would imply that steam-water flow cannot be characterized by the porous medium approach. The equivalent homogeneous single-phase approach to model steam-water flow in fracture is under investigation. Also, alternative ways for calculating steam and water flow rates using energy balance and tracking bubble movement methods are being evaluated.

The future work will focus on the steady-state steam-water relative permeability experiment. In order to compare steam-water and nitrogen-water behavior, a nitrogen-water relative permeability experiment is planned under the same conditions as the steam-water experiment (high temperature, high flow rate, same analysis method). After that the rough-wall steam-water relative permeability experiment will be conducted.

## 2. EXPERIMENTAL VERIFICATION OF CAPILLARY PRESSURE TECHNIQUES TO CALCULATE RELATIVE PERMEABILITY

This research project is being conducted by Research Associate Kewen Li and Professor Roland Horne. The objective of this project is to further verify the methods to calculate relative permeability using experimental capillary pressure data.

### 2.1 SUMMARY

The Brooks-Corey model has been accepted widely to calculate relative permeability using capillary pressure data. However the Purcell model was found to be the best fit to the experimental data of the wetting phase relative permeability for the cases studied, as long as the measured capillary pressure curve had the same residual saturation as the relative permeability curve. The differences between the experimental and the Purcell model data were almost negligible. A physical model was developed to explain the insignificance of the effect of tortuosity on the wetting-phase. For nonwetting phase relative permeability, the model results were very close to the experimental values in drainage except for the Purcell model. However, calculated data in imbibition were different than the experimental data. This study showed that relative permeability could be calculated satisfactorily by choosing a suitable capillary pressure technique, especially in drainage processes. In the reverse procedure, capillary pressure could also be computed once relative permeability data are available.

### 2.2 INTRODUCTION

Relative permeability is of central importance to reservoir engineering but difficult to measure in some cases. Such cases include extremely low permeability rocks and fluid systems in which there are phase transformation and mass transfer between the two phases as pressure changes. Steam-water flow in geothermal rock is an example of such a system. Steam-water relative permeability plays an important role in controlling reservoir performance for water injection into geothermal reservoirs. At the same time, Li and Horne (2001a) found significant differences between steam-water and air-water capillary pressures, and Horne *et al*. (2000) found differences between steam-water and air-water relative permeabilities. According to these studies, steam-water flow properties may not be replaced simply by air-water or nitrogen-water flow properties. It would be helpful for reservoir engineers to be able to calculate steam-water relative permeability once steam-water capillary pressure data are available.

There are many papers related to techniques for the calculation of relative permeabilities from capillary pressure data. Purcell (1949) developed a method to calculate the permeability using pore size distribution derived from mercury-injection capillary pressure curves. This method was used to calculate the multiphase relative permeabilities, as reported by Gates and Leits (1950). Later, Burdine (1953) introduced a tortuosity factor in the model. Corey (1954) and Brooks and Corey (1966) summarized the previous works and modified the method by representing capillary pressure curve as a power law function of the wetting phase saturation. Honarpour *et al*. (1986) reviewed the literature in this field. The published literature and experimental data for relative permeability and

capillary pressure were not sufficient to conclude which method should be the standard approach.

Unlike for oil-gas and oil-water flow properties, there are few studies for the calculation of steam-water relative permeabilities by the capillary pressure technique. Historically, the capillary pressure techniques were developed for drainage situations and were useful to obtain gas-liquid (oil or water) relative permeability when fluid flow tests were not practical.

In this study, we calculated the gas-liquid (including gas-oil, air-water, and steam-water) and oil-water relative permeabilities using experimental data of capillary pressure from different rocks by different methods such as the Purcell, Burdine, Corey, and Brooks-Corey methods. The calculated results were compared to the relative permeability data measured in the same core sample. The purpose of this study was to verify which capillary pressure technique would achieve the best fit to the experimental data of relative permeability.

## 2.3 THEORY

We chose four representative models developed by various authors to calculate steam-water relative permeabilities from capillary pressure measurements. The mathematical expressions of the four models are described in this section.

### *Purcell Model*

Purcell (1949) developed an equation to compute rock permeability by using capillary pressure data. This equation can be extended to the calculation of multiphase relative permeability. In two-phase flow, the relative permeability of the wetting phase can be calculated as follows:

$$k_{rw} = \frac{\int_0^{S_w} dS_w / (P_c)^2}{\int_0^1 dS_w / (P_c)^2} \tag{2.1}$$

where $k_{rw}$ and $S_w$ are the relative permeability and saturation of the wetting phase; $P_c$ is the capillary pressure as a function of $S_w$.

Similarly, the relative permeability of the nonwetting phase can be calculated as follows:

$$k_{rnw} = \frac{\int_{S_w}^1 dS_w / (P_c)^2}{\int_0^1 dS_w / (P_c)^2} \tag{2.2}$$

where $k_{rnw}$ is the relative permeability of the nonwetting phase. It can be seen from Eqs. 2.1 and 2.2 that the sum of the wetting and nonwetting phase relative permeability at a specific saturation is equal to one. This may not be true in most porous media. In the next section, the relative permeabilities calculated using this method are compared to

experimental data. The comparison shows that Eq. 2.1 is close to experimental values of the wetting phase relative permeability but Eq. 2.2 is far from the experimental results.

***Burdine Model***

Burdine (1953) developed equations similar to Purcell's method by introducing a tortuosity factor as a function of wetting phase saturation. The relative permeability of the wetting phase can be computed as follows:

$$k_{rw} = (\lambda_{rw})^2 \frac{\int_0^{S_w} dS_w/(P_c)^2}{\int_0^1 dS_w/(P_c)^2} \tag{2.3}$$

where $\lambda_{rw}$ is the tortuosity ratio of the wetting phase. According to Burdine (1953), $\lambda_{rw}$ could be calculated as follows:

$$\lambda_{rw} = \frac{\tau_w(1.0)}{\tau_w(S_w)} = \frac{S_w - S_m}{1 - S_m} \tag{2.4}$$

where $S_m$ is the minimum wetting phase saturation from the capillary pressure curve; $\tau_w$ (1.0) and $\tau_w$ ($S_w$) are the tortuosities of the wetting phase when the wetting phase saturation is equal to 100% and $S_w$ respectively.

In the same way, relative permeabilities of the nonwetting phase can be calculated by introducing a nonwetting phase tortuosity ratio. The equation can be expressed as follows:

$$k_{rnw} = (\lambda_{rnw})^2 \frac{\int_{S_w}^1 dS_w/(P_c)^2}{\int_0^1 dS_w/(P_c)^2} \tag{2.5}$$

where $k_{rnw}$ is the relative permeability of the nonwetting phase; $\lambda_{rnw}$ is the tortuosity ratio of the nonwetting phase, which can be calculated as follows:

$$\lambda_{rnw} = \frac{\tau_{nw}(1.0)}{\tau_{nw}(S_w)} = \frac{1 - S_w - S_e}{1 - S_m - S_e} \tag{2.6}$$

here $S_e$ is the equilibrium saturation of the nonwetting phase; $\tau_{nw}$ is the tortuosity of the nonwetting phase.

Honarpour *et al*. (1986) pointed out that the expression for the wetting phase relative permeability (Eq. 2.3) fits the experimental data much better than the expression for the nonwetting phase (Eq. 2.5).

***Corey Model***

According to the Purcel and Burdine models, an analytical expression for the wetting and nonwetting phase relative permeabilities may be obtained if capillary pressure curves can be represented by a simple mathematical function. Corey (1954) found that oil-gas capillary pressure curves could be expressed approximately using the following linear relation:

$$1/P_c^2 = CS_w^* \tag{2.7}$$

where C is a constant and $S_w^*$ is the normalized wetting phase saturation expressed as follows:

$$S_w^* = \frac{S_w - S_{wr}}{1 - S_{wr}} \tag{2.8a}$$

where $S_{wr}$ is the residual saturation of the wetting phase or water phase in steam-water flow. In Corey's case, $S_{wr}$ is the residual oil saturation.

Although originally the Corey model was not developed for the imbibition case, in this study it was used to calculate the imbibition steam-water relative permeabilities by defining the normalized wetting phase saturation as follows:

$$S_w^* = \frac{S_w - S_{wr}}{1 - S_{wr} - S_{nwr}} \tag{2.8b}$$

where $S_{nwr}$ is the residual saturation of the nonwetting phase, representing the residual steam saturation in this study.

Substituting Eq. 2.7 into Eqs. 2.3 and 2.5 with the assumption that $S_e$=0 and $S_m$=$S_{wr}$, Corey (1954) obtained the following equations to calculate the wetting (oil) and nonwetting (gas) phase relative permeabilities for drainage cases:

$$k_{rw} = (S_w^*)^4 \tag{2.9}$$

$$k_{rnw} = (1 - S_w^*)^2[1 - (S_w^*)^2] \tag{2.10}$$

A constraint to the use of Corey's model (Eqs. 2.9 and 2.10) is that the capillary pressure curve can be represented by Eq. 2.7.

***Brooks-Corey Model***

Because of the limitation of Corey's model, Brooks and Corey (1966) modified the representation of capillary pressure function to a more general form as follows:

$$P_c = p_e (S_w^*)^{-1/\lambda} \tag{2.11}$$

where $p_e$ is the entry capillary pressure and $\lambda$ is the pore size distribution index.

Substituting Eq. 2.11 into the Burdine model (Eqs. 2.3 and 2.5) with the assumption that $S_e$=0, Brooks and Corey (1966) derived equations to calculate the wetting and nonwetting phase relative permeabilities as follows:

$$k_{rw} = (S_w^*)^{\frac{2+3\lambda}{\lambda}} \tag{2.12a}$$

$$k_{rnw} = (1 - S_w^*)^2 [1 - (S_w^*)^{\frac{2+\lambda}{\lambda}}] \tag{2.12b}$$

When $\lambda$ is equal to 2, the Brooks-Corey model is reduced to the Corey model.

## 2.4 RESULTS

The experimental data of capillary pressure from our previous study and the literature were used in this paper. The calculation and comparison in steam-water, nitrogen-water, oil-water, and oil-gas flow are presented and discussed in this section.

### 2.4.1 Steam-Water Flow

The data of both drainage and imbibition steam-water capillary pressure from Li and Horne (2001b) were used to calculate the corresponding steam-water relative permeability. Note that the capillary pressure data were represented using Eq. 2.11 in all the calculations by the Purcell model. The calculated results were compared to the experimental data of steam-water relative permeability (Mahia, 1999). Figure 2.1 shows the experimental data of the steam-water relative permeability and capillary pressure in drainage. All these data were measured at a temperature of about 120$^o$C in the same Berea core sample. Because the relative permeability and the capillary pressure were measured simultaneously, the two curves had the same residual water saturations. This feature is important and will be discussed in more detail later. Note that the steam relative permeability data shown in Figure 2.1 have been calibrated under the consideration of gas slippage in two-phase flow by Li and Horne (2001c).

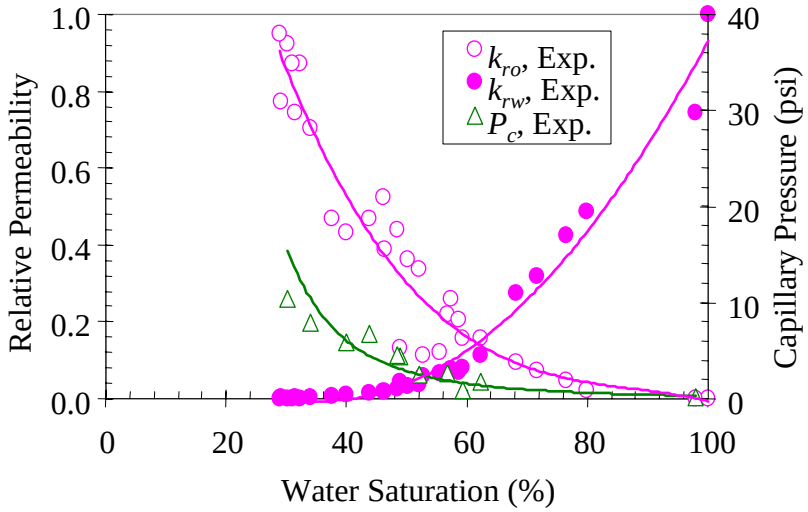


*Figure 2.1: Experimental data of drainage steam-water relative permeability and capillary pressure (Mahia, 1999; Li and Horne, 2001b).*

The drainage steam-water relative permeabilities were calculated using the experimental data of the drainage steam-water capillary pressure shown in Figure 2.1 and plotted versus the normalized water saturation that is defined in Eq. 2.8a. The calculated results and the comparison to the corresponding experimental data are shown in Figure 2.2. The water relative permeabilities calculated using the Purcell model are the best fit to the experimental data. This implies that it may not be necessary to adjust the calculation of the wetting phase relative permeabilities by introducing the concept of the tortuosity factor in such a case. The water phase relative permeabilities calculated by all the other models are less than the experimental values. It can be seen from Figure 2.2 that the steam phase (nonwetting phase) relative permeabilities calculated by all the models but the Purcell model are almost the same and consistent with the experimental data for the drainage case. The steam phase relative permeabilities calculated by the Purcell model are not shown in Figure 2.2 and all the figures following in this section because the curve is concave to the axis of the normalized water saturation on the Cartesian plot, which is unexpected and far from the experimental values.

The experimental data of the imbibition steam-water relative permeability and the imbibition capillary pressure are shown in Figure 2.3. These data were also measured simultaneously in the same Berea core sample at a temperature of about 120$^{o}$C. The steam relative permeability data shown in Figure 2.3 have been calibrated under the consideration of gas slippage in two-phase flow.

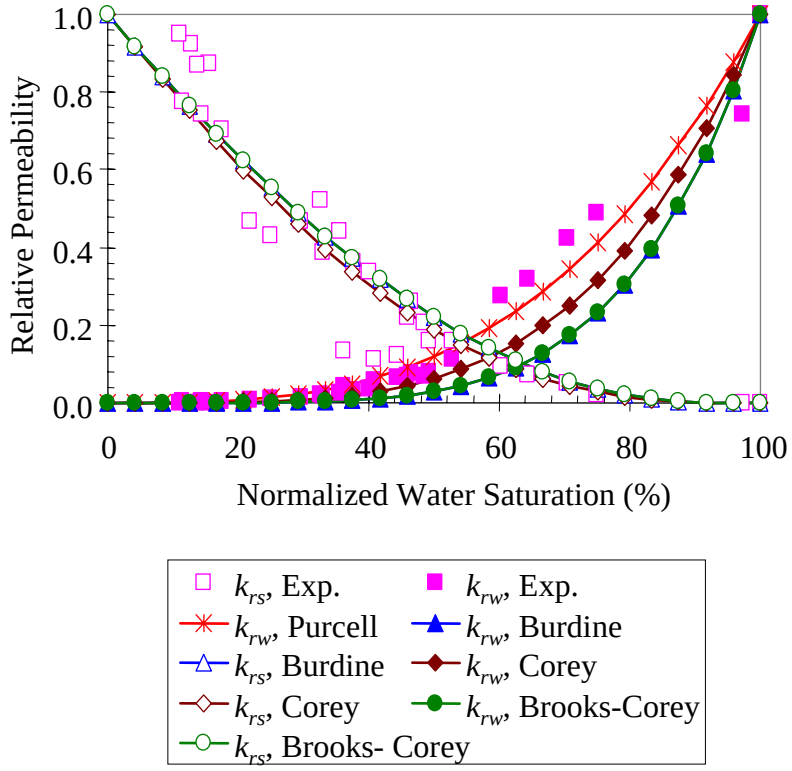


*Figure 2.2: Calculated steam-water relative permeability and the comparison to the experimental data in drainage case.*

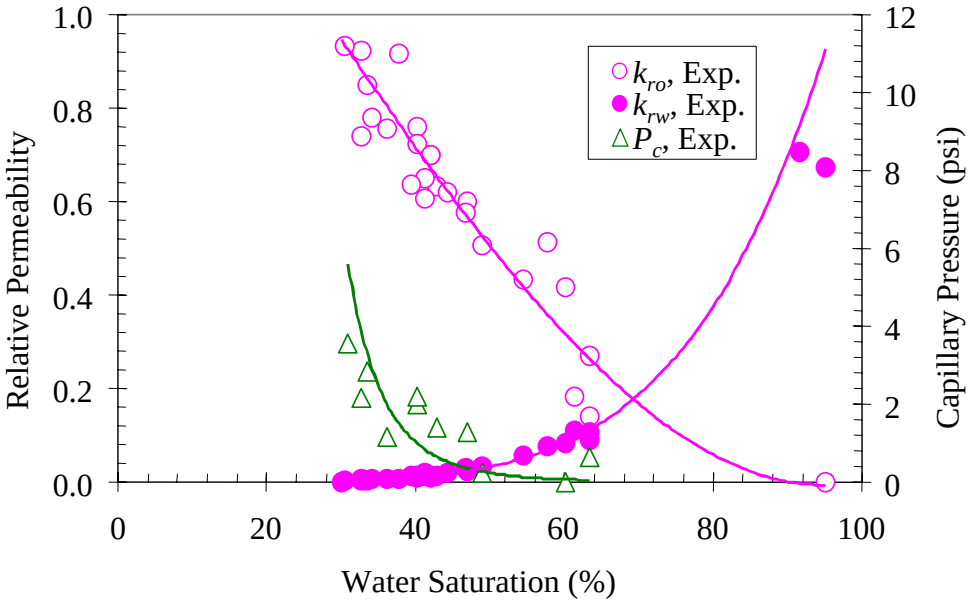


*Figure 2.3: Experimental data of imbibition steam-water relative permeability and capillary pressure (Mahia, 1999; Li and Horne, 2001b).*

The imbibition steam-water relative permeabilities were then calculated using the measured data of the imbibition steam-water capillary pressure shown in Figure 2.3 and also plotted versus the normalized water saturation. Figure 2.4 shows the calculated results and the comparison to the experimental values. The water relative permeabilities from the Purcell model are still the best fit to the experimental data. The results from the Corey model are a good fit too. The water phase relative permeabilities calculated by the Burdine and the Brooks-Corey models are less than the experimental values. Actually the results calculated using the two models are the same if the capillary pressure data in the Burdine model are represented using Eq. 2.11. The steam phase relative permeabilities calculated by all the models except the Purcell model are not significantly different from each other but are much less than the experimental data for the imbibition case.

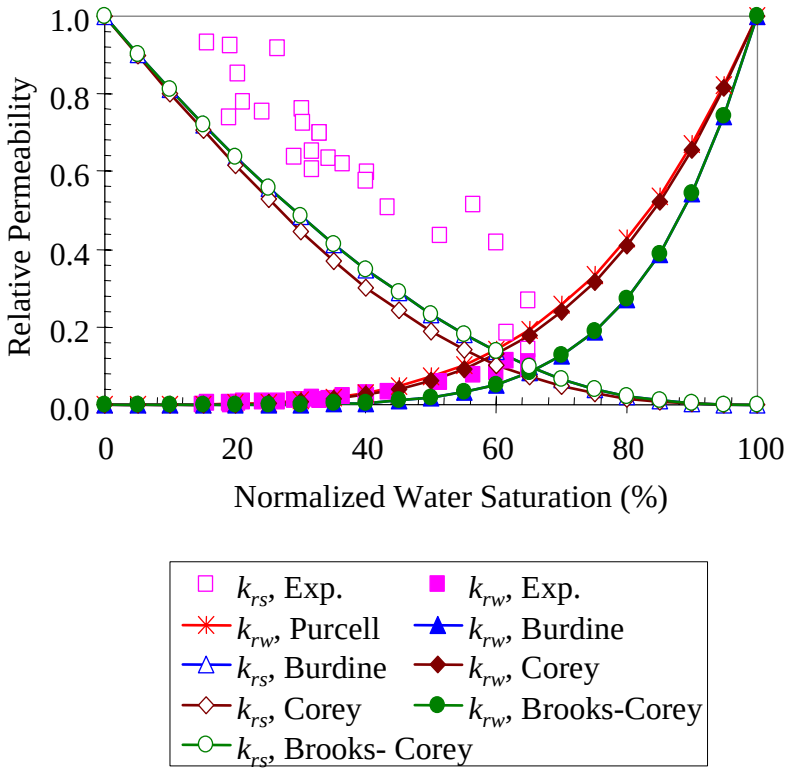


*Figure 2.4: Calculated steam-water relative permeability and the comparison to the experimental data in imbibition case.*

### 2.4.2 Nitrogen-Water Flow

In the following section, we will discuss the calculated results and the comparison in nitrogen-water systems. Li and Horne (2001c) measured the nitrogen-water relative permeabilities in a fired Berea core sample similar to that used in the measurement of steam-water relative permeabilities by Mahiya (1999). In this study, we drilled a plug from another part of the same fired Berea sandstone that was used by Li and Horne (2001c). The length and diameter of the plug sample were 5.029 cm and 2.559 cm respectively; the porosity was 24.37%. The drainage nitrogen-water capillary pressure of the plug was measured by using the semipermeable porous-plate method. The measured

data of the drainage nitrogen-water capillary pressure along with the relative permeabilities by Li and Horne (2001c) are plotted in Figure 2.5. Although the capillary pressure and relative permeability curves were not measured simultaneously, the residual water saturations were the same for both.

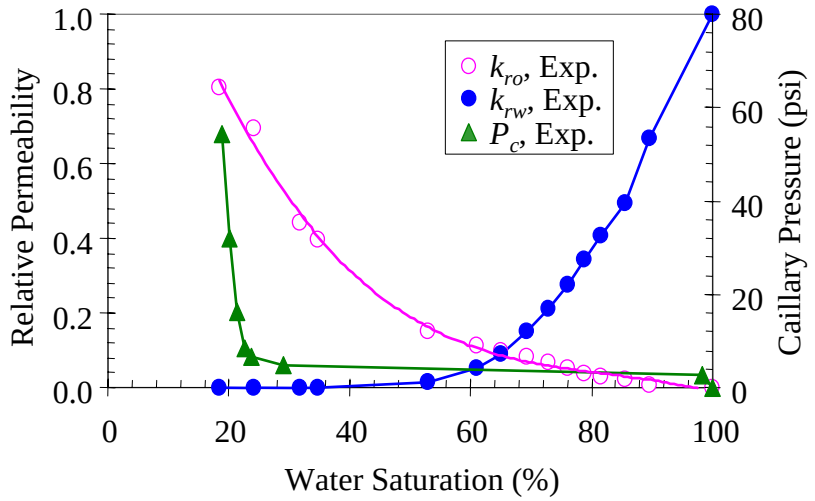


*Figure 2.5: Drainage nitrogen-water relative permeability and capillary pressure.*

The results calculated using the capillary pressure models for the nitrogen-water flow (drainage) and the comparison to the experimental data are shown in Figure 2.6. The experimental data of water relative permeability are located between the Purcell model and the Corey model. The two models provide a good approximation to the experimental data in this case. The features of gas phase relative permeability curve calculated by these models are similar to those of steam-water flow (see Figure 2.4) except that the calculated results are greater than the measured data.

### 2.4.3 Oil-Water Flow

Kleppe and Morse (1974) reported the experimental data of imbibition oil-water relative permeability and capillary pressure in Berea sandstone with a permeability of 290 md and a porosity of 22.5%. The three curves are shown in Figure 2.7. The calculated results of oil and water relative permeability and the comparison to the experimental data are plotted in Figure 2.8. In oil-water flow, the best fit to the wetting phase (water phase in this case) relative permeability is also from the Purcell model. The water phase relative permeabilities calculated using other models are not notably different from each other but are much less than the experimental data in this case. For the nonwetting phase (oil phase in this case) relative permeability, all the models except the Purcell model give good fit to the experimental data.

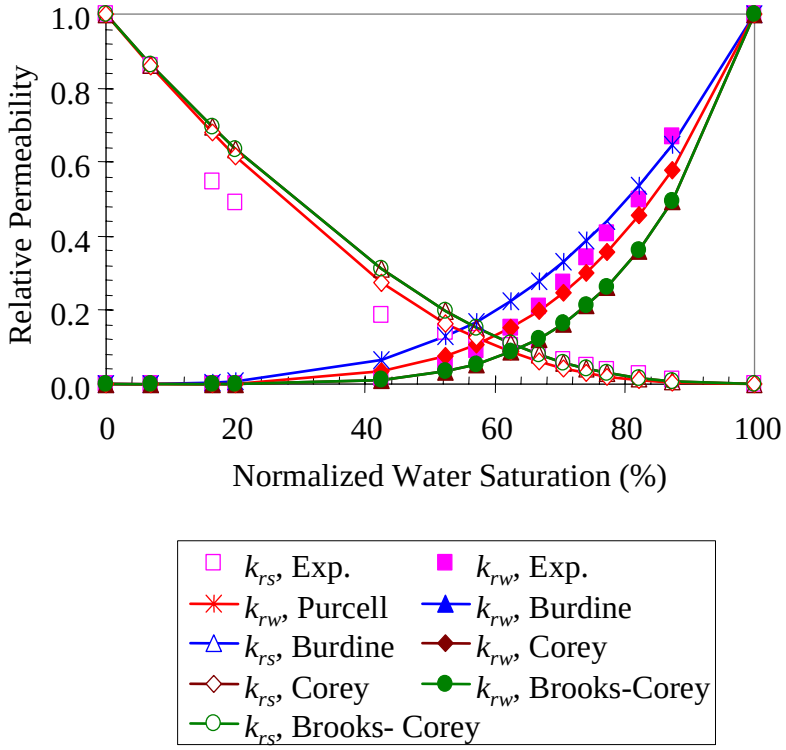


*Figure 2.6: Calculated nitrogen-water relative permeability and the comparison.*

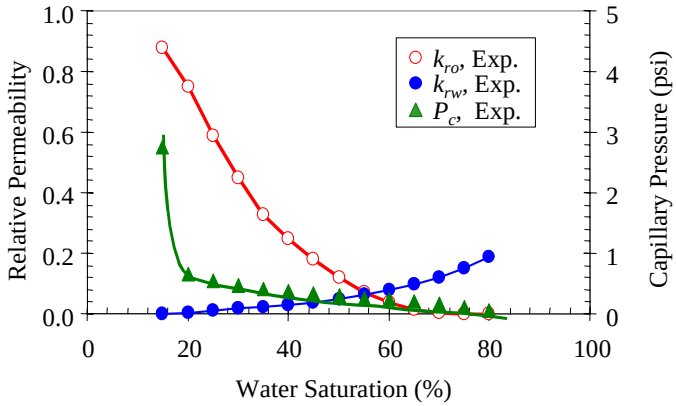


*Figure 2.7: Imbibition oil-water relative permeability and capillary pressure from Kleppe and Morse (1974).*

Beckner *et al*. (1988) reported imbibition oil-water relative permeability and capillary pressure data which were representative of actual field data (see Figure 2.9). The capillary pressure data were also used to calculate oil-water relative permeability with various methods. The results and the comparison are shown in Figure 2.10. The Purcell model produced the best fit to the water phase relative permeability, the same as observed previously. The water phase relative permeabilities calculated using other models are less than the relative permeability data from Beckner *et al*. (1988).

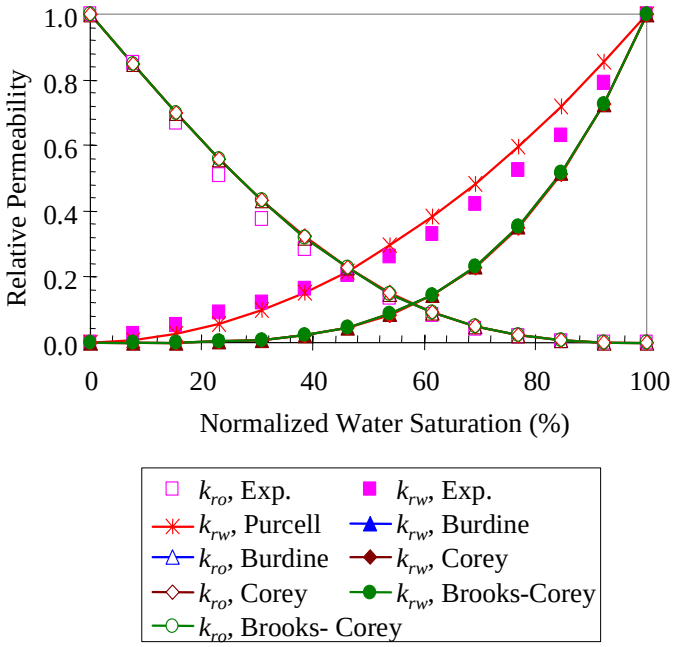


*Figure 2.8: Calculated oil-water relative permeability and the comparison to the experimental data from Kleppe and Morse (1974).*

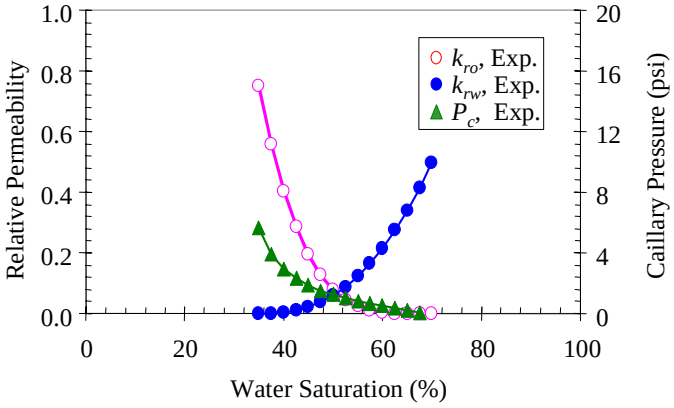


*Figure 2.9: Imbibition oil-water relative permeability and capillary pressure from Beckner et al. (1988).*

### 2.4.4 Oil-Gas Flow

We made the same calculation and comparison using the data of oil-gas relative permeability and capillary pressure measured in Berea sandstone by Richardson *et al.* (1952). The permeability and porosity of this core were 107 md and 17.7%; the length and diameter were 30.7 cm and 6.85 cm, respectively. The oil phase was kerosene and the gas phase was helium. The experimental data of the drainage oil-gas relative permeability and the capillary pressure are shown in Figure 2.11. The calculated results of relative permeability and the comparison to the experimental values are demonstrated in Figure 2.12. We also observed that the best fit to the wetting phase relative permeability in oil-gas flow was from the Purcell model.

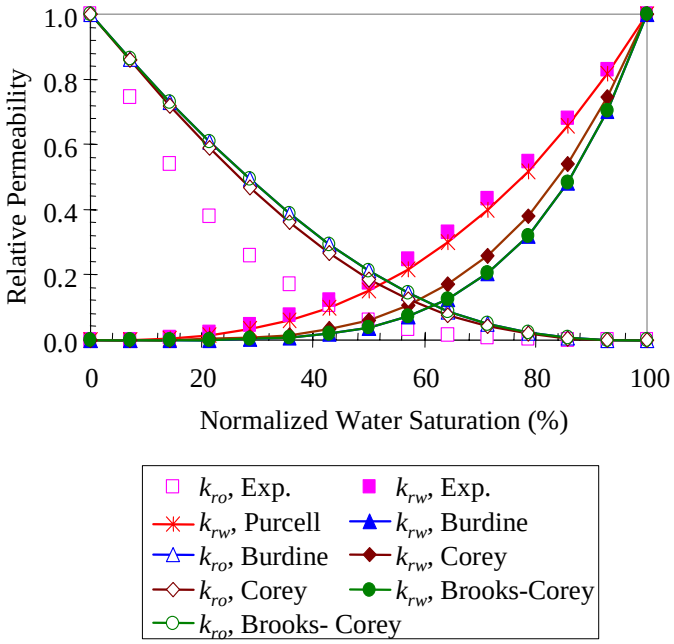


*Figure 2.10: Calculated oil-water relative permeability and the comparison to the data from Beckner et al. (1988).*

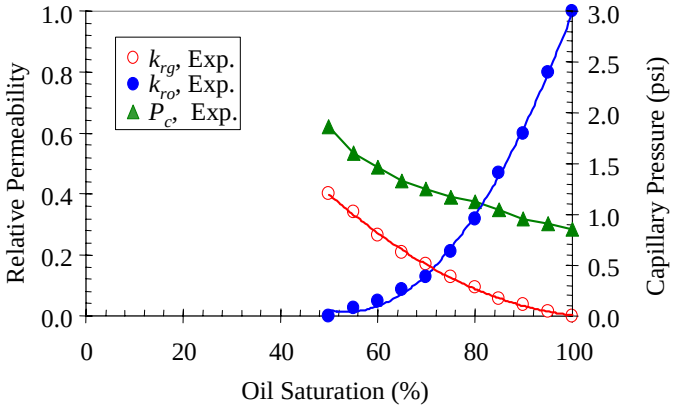


*Figure 2.11: Drainage oil-gas relative permeability and capillary pressure from Richardson et al. (1952).*

All the relative permeability and capillary pressure curves we used in the previous sections have a common feature: the residual saturation from the capillary pressure curve is equal to that from the relative permeability curve. Gates and Lietz (1950) reported oil-gas relative permeability and capillary pressure curves without such a feature. The experimental data of drainage oil-gas relative permeability and capillary pressure, taken from Figure 2.4 in the paper by Gates and Lietz (1950), were used in this study and are depicted in Figure 2.13. These data were measured in a Pyrex core with a permeability of 1370 md and a porosity of 37.4%. The oil phase was kerosene and the gas phase was air. The residual oil saturation was about 30% according to the oil phase relative permeability curve but was about 12% according to the capillary pressure and the gas phase relative permeability curves (see Figure 2.13). The reason might be the evaporation of oil caused

by continuous gas injection even after the residual oil saturation by displacement was reached.

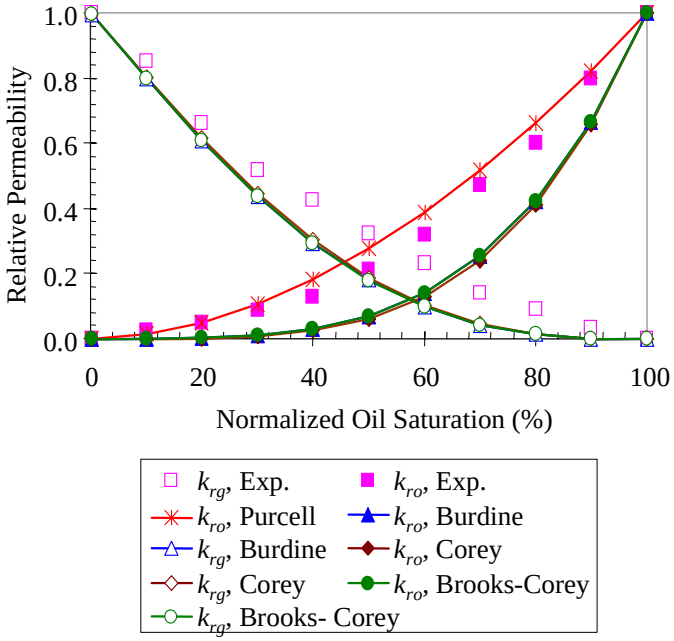


*Figure 2.12: Calculated oil-gas relative permeability and the comparison to the experimental data from Richardson et al. (1952).*

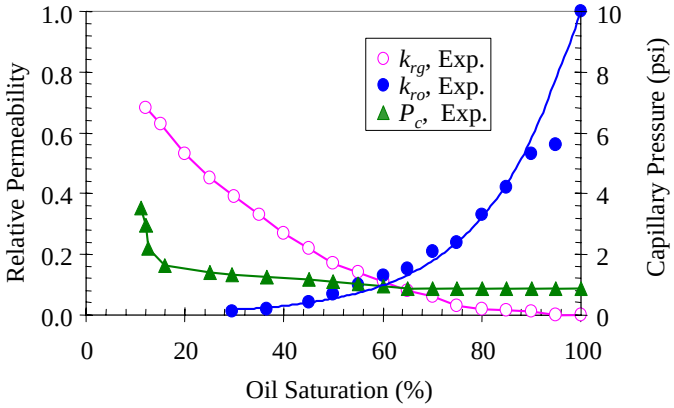


*Figure 2.13: Drainage oil-gas relative permeability and capillary pressure from Gates and Lietz (1950).*

The oil and gas relative permeabilities calculated using various capillary pressure techniques were compared to the experimental data measured by Gates and Lietz (1950) and the results are demonstrated in Figure 2.14. We observed that all the models except the Purcell model yielded the best fit to both the wetting and nonwetting phase relative permeabilities.

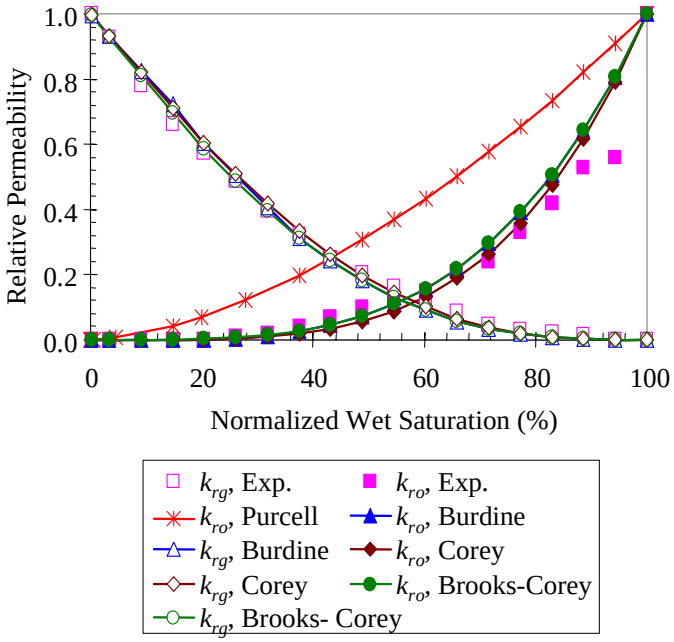


*Figure 2.14: Calculated oil-gas relative permeability and the comparison to the experimental data from Gates and Lietz (1950).*

In summarizing all the calculations that we have made, including some not presented here, the Purcell model was the best fit to the wetting phase relative permeability if the measured capillary pressure curve had the same residual saturation as the relative permeability curve.

### 2.4.5 Calculation of capillary pressure using relative permeability data

In some cases, relative permeability data are available but capillary pressure data are not. A method to calculate capillary pressure function using relative permeability is proposed in this section. As observed previously, the Purcell model may be the best fit to the experimental data of the wetting phase relative permeability. Substituting $P_c$ using Eq. 2.12, the Purcell model can be expressed as follows:

$$k_{rw} = (S_w^*)^{\frac{2+\lambda}{\lambda}} \qquad (15)$$

Therefore we can fit the experimental data of the wetting phase relative permeability using Eq. 2.15 to obtain the value of the pore size distribution index λ. According to Eq. 2.12, the corresponding capillary pressure function can be determined once the value of the pore size distribution index λ is available. The entry capillary pressure may be measured readily or can be evaluated using other methods

## 2.5 DISCUSSION

The techniques using capillary pressure to calculate relative permeability were developed in the late forties. Burdine (1953) pointed out that the calculated relative permeabilities

are more consistent and probably contain less maximum error than the measured data because the error in measurement is unknown. This may be true in some cases. However, the differences between different capillary pressure models are obvious, especially for the wetting phase. Therefore, one important question is which model is most appropriate for practical use. The calculations in this study showed that the Purcell model was the best fit to the wetting phase relative permeability. This seems surprising because the concept of the tortuosity factor as a function of wetting phase saturation is not introduced for the calculation of the wetting phase relative permeability in such a case. A physical model was developed to demonstrate the insignificant effect of the tortuosity factor on the wetting phase, as shown in Figure 2.15. $L$ is the direct distance between the ends of a single capillary tube and $L_a$ is the length of the tortuous capillary tube.

Burdine (1953) obtained an empirical expression of the effective tortuosity factor as a function of wetting phase saturation (see Eq. 2.4). $\lambda_{rw}$ is actually the ratio of the tortuosity at 100% wetting phase saturation to the tortuosity at a wetting phase saturation of $S_w$. According to Eq. 2.4, the tortuosity of wetting phase is infinite at the minimum wetting phase saturation that is equal to residual water saturation $S_{wr}$ here. This may not be true for the wetting phase because the wetting phase may exist on the rock surface in the form of continuous film, as shown in Figure 2.15b. In this case, $\tau_w$ ($S_m = S_{wr}$) may be close to $\tau_w$ (1.0) (see Figure 2.15a), which demonstrates that there is little effect of the wetting phase saturation on the tortuosity of the wetting phase. Similarly, based on Eq. 2.6, the tortuosity of the nonwetting phase is infinite when the wetting phase saturation is equal to 1-$S_e$. This may be true because the nonwetting phase may exist in the form of discontinuous droplets (see Figure 2.15c). In this case, $S_e$ is equal to $S_{gr}$.

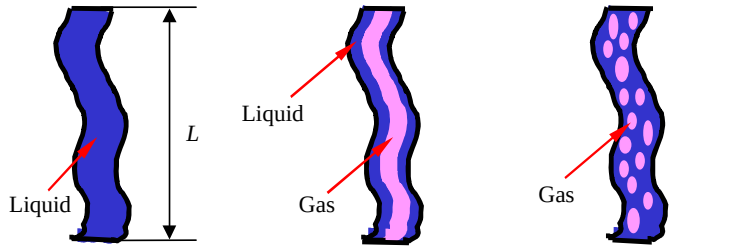


(a) $S_w = 100\%$ $\tau_w(S_w) = (\frac{L_a}{L})^2$

(b) $S_w = S_{wr}$ $\tau_w(S_w) \approx (\frac{L_a}{L})^2$

(c) $S_w = 1\text{-}S_{gr}$ $\tau_w(S_w) = \infty$

*Figure 2.15: Tortuosity in a single capillary tube.*

It can be seen from the analysis here that the tortuosity of wetting and nonwetting phases would behave differently as a function of wetting phase saturation. This may be why it is necessary to introduce the tortuosity for the nonwetting phase but not for the wetting phase.

As stated previously, capillary pressure techniques were developed originally in cases in which it is difficult to measure relative permeability. Actually these techniques may also

be useful even in cases in which both relative permeability and capillary pressure data are available. In these cases, we can still calculate relative permeability using the appropriate models with the capillary pressure data and compare the results to the experimental values. If the calculated results are consistent with the experimental data, we may have more confidence on the experimental measurements. This idea may also be applied to numerical simulation. For example, it may be helpful to check the relative permeability curves obtained from upscaling using the capillary pressure techniques.

## 2.6 CONCLUSIONS

Based on the present study, the following conclusions may be drawn:

1. The calculated results in gas-liquid and oil-water flow indicate that the Purcell model may be the best fit to the experimental data of the wetting phase relative permeability for both drainage and imbibition processes but is not a good fit for the nonwetting phase.
2. It may not be necessary to introduce the tortuosity factor in calculating the wetting phase relative permeability as long as the measured capillary pressure curve had the same residual saturation as the relative permeability curve.
3. Except for the Purcell model, the results of the nonwetting phase relative permeability calculated using the models for the drainage case were almost the same and very close to the experimental values. However, those for the imbibition cases were different from the measured data.
4. The capillary pressure techniques would be valuable not only in cases in which it is difficult to measure relative permeability curves but also in cases in which both relative permeability and capillary pressure data are available.
5. In general, the Purcell model is proposed to calculate the wetting phase relative permeability and the Brooks-Corey model is proposed to calculate the nonwetting phase relative permeability once reliable capillary pressure data are available.

## 3. FRACTURED ROCK RELATIVE PERMEABILITY

This project is being conducted by Research Assistant Mark D. Habana, Research Associate Kewen Li and Prof. Roland N. Horne. The objective is to measure relative permeability relations for nitrogen and water flow in a fractured geothermal rock. This work is an extension of current studies of nitrogen-water and steam-water flows, which have so far considered only artificially uniform porous rock. This quarter, a new 2 inch diameter core was used in nitrogen-water relative permeability experiments. Prior to this, an experiment was conducted to determine the resistivity and saturation relationship for this core. Also, the absolute permeability of the core was obtained using single-phase water flow.

### 3.1 BACKGROUND

Various works on flow through fractures have shown different kinds of relative permeability behavior. Experimental studies by Persoff and Pruess (1995) resulted in curves that cannot be classified either as Corey type or as linear (X-curve) type. Fourar et al. (1993) suggested that multiphase interaction in a fracture is a function of flow velocity and therefore that relative permeability is not the appropriate way to describe multiphase flow in fractures.

Past experiments have used synthetic fabricated fractures and/or gas-water or oil-water as fluids. This experimental study is using a real fractured rock core from The Geysers geothermal field to study relative permeability.

Nitrogen and helium permeability experiments were conducted on the core to determine the effects of the rock fractures and to investigate the constraints and practicalities of conducting multiphase flow experiments in real geothermal rocks. The core contains several fractures as determined from an X-ray computer tomography image.

### 3.2 EXPERIMENTAL METHODOLOGY

The rock permeability was measured using nitrogen and helium gas at room temperature. Since gas permeability is a function of pressure, as described by Equation 3.1, the flow measurements were conducted at a series of different mean pressures.

$$k_{gas} = k_{abs}\left(1 - \frac{b}{p_{ave}}\right) \tag{3.1}$$

The core sample was obtained from a depth of 1409.3 m at The Geysers geothermal field. It is 4.70 cm in length and 6.91 cm in diameter.

At different confining pressures nitrogen was flowed into the core. Confining pressure from 500 to 850 psig was applied by injecting nitrogen around the heat shrink tubing inside the core holder. To apply a confining pressure of 1150 psig, water was used in place of nitrogen.

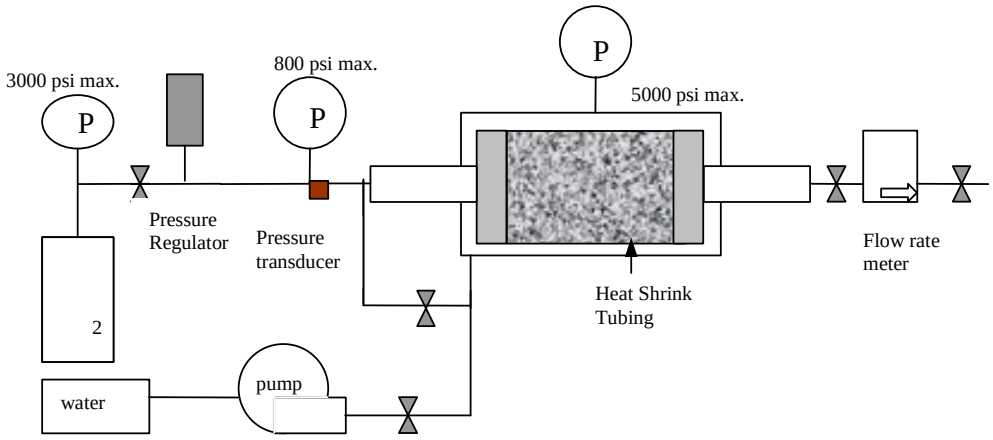


*Figure 3.1: Apparatus for flow measurement in geothermal rock.*

A pressure gauge and a pressure transducer connected to a digital display measured pressure at the inlet. The pressure at the outlet was taken to be 1 atm. The flow rate at the outlet was measured using a Matheson flow rate meter and controller (Model 8272-MF2000). The flow rate transducer calibration equation used was that determined by Kewen Li when he used the device in his experiments on slip factors (Oct-Dec 1999 Quarterly Report).

A new 2 inch diameter and 2 inch length core was cut from The Geysers geothermal rock obtained at a depth of 1450 metres.

To determine the resistivity-saturation correlation for The Geysers core using two metal endplates, the apparatus shown in Figure 3.2 was used.

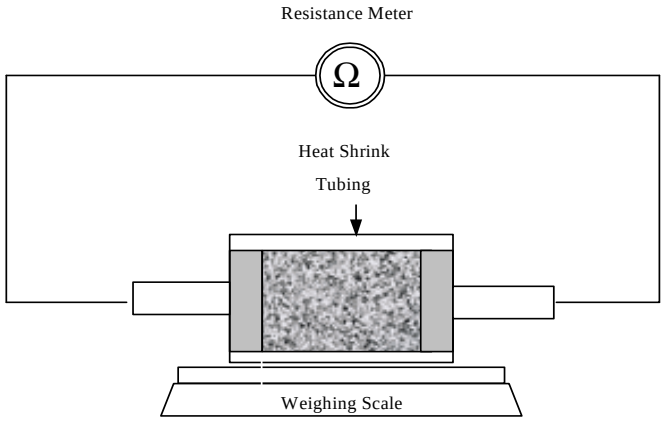


*Figure 3.2: Apparatus for determining resistivity-saturation correlation in geothermal rock.*

The core was saturated fully with water and then wrapped with rubber sheet, with the two metal plates attached on both ends of the core. The core was then allowed to dry on a weighing scale. Resistance measurements were measured as the mass of the saturated core decreased. Resistivity and resistivity indices were calculated for each resistance reading by using Equation 3.2 and 3.3.

$$\rho = r(\frac{A}{L}) \tag{3.2}$$

$$R_{index} = \frac{\rho_{partiallysaturated}}{\rho_{fullysaturated}} \tag{3.3}$$

where $r$ is resistance

$A$ is area

$L$ is length

ρ is resistivity

The absolute permeability of the core was obtained by pumping liquid water into the core until steady state was achieved. Darcy's law was applied to calculate the absolute permeability value.

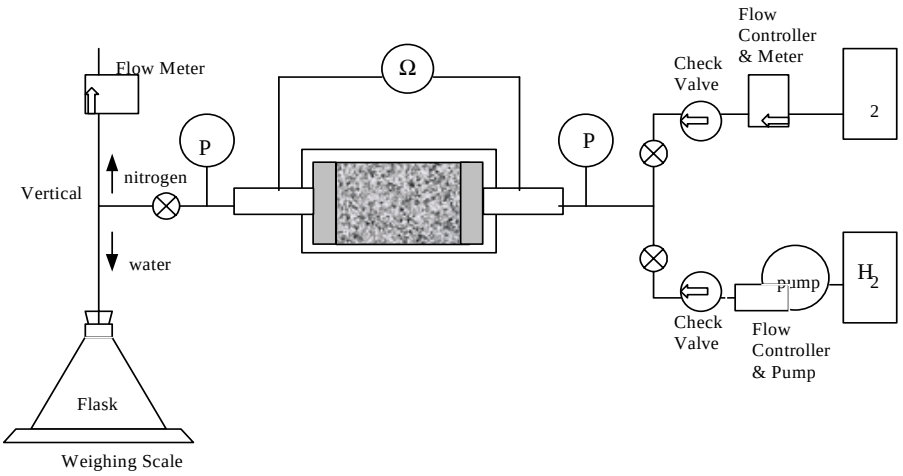


*Figure 3.3: Apparatus for nitrogen-water relative permeability experiment. Pressure transducers, flowmeters, and the weighing scale are connected to an automated data acquisition system.*

Constant flowrate nitrogen-water relative permeability experiments were done. Difficulties in achieving steady state were encountered and so the experiment was changed to constant nitrogen gas pressure and constant water flowrate. The data acquisition system was automated using a PCI-6024E board and an SCB-68 shielded connector block; both manufactured by National Instruments. Resistance measurements were taken at the end of the experiment runs for use in determining the water saturation.

## 3.3 PARTIAL RESULTS AND DISCUSSION

Results of the nitrogen permeability experiments are shown in Figure 3.4.

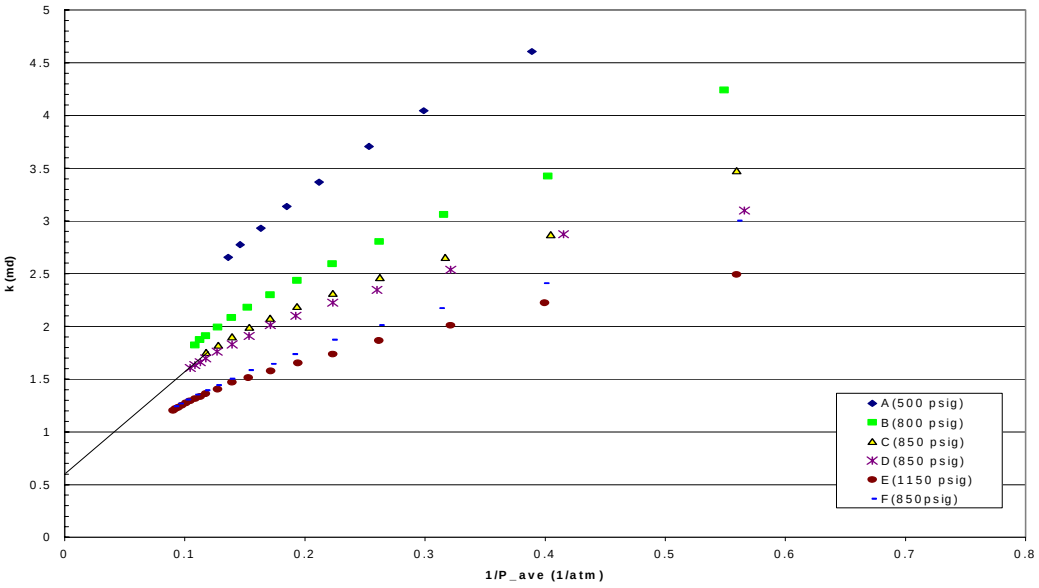


*Figure 3.4: Nitrogen permeability as a function of pressure.*

The intersection of the extrapolated lines with the vertical axis in the plot of permeability ($k$) versus the reciprocal of the mean pressure ($1/p_{ave}$) is taken to be the absolute permeability of the rock. At a confining pressure of 850 psig the absolute permeability is approximately 0.56 md.

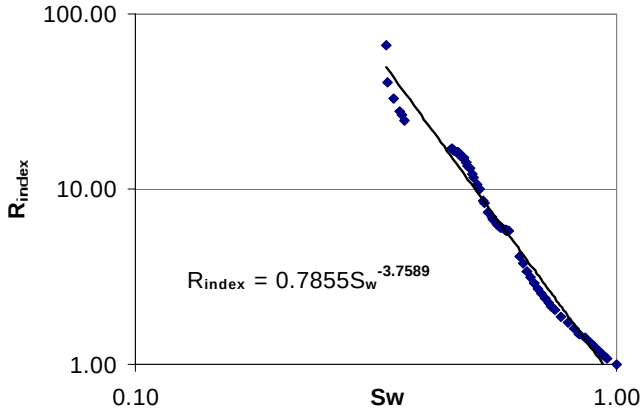


*Figure 3.5: Resistivity index vs. saturation for geothermal core.*

Results of the resistivity-saturation experiment are shown in Figure 3.5. A linear relationship is evident between the resistivity index and the water saturation in a log-log

plot. Resistance measurements exceed the sensitivity of the resistance meter at water saturations below 33%.

Steady state was achieved in the absolute permeability experiment, using water, at a flowrate of 9.9 ml/min and a pressure gradient of 658 psi. The calculated absolute permeability for the 2 inch diameter core is 0.23 md. This is lower than the 0.5 md obtained by extrapolation in the nitrogen absolute permeability experiment.

Constant flowrate nitrogen-water relative permeability experiments were conducted. Steady-state was not achieved in these experiments. Pressure spikes of 100 psi, shown in Figure 3.6, remain even if the general pressure trend tends to stabilize.

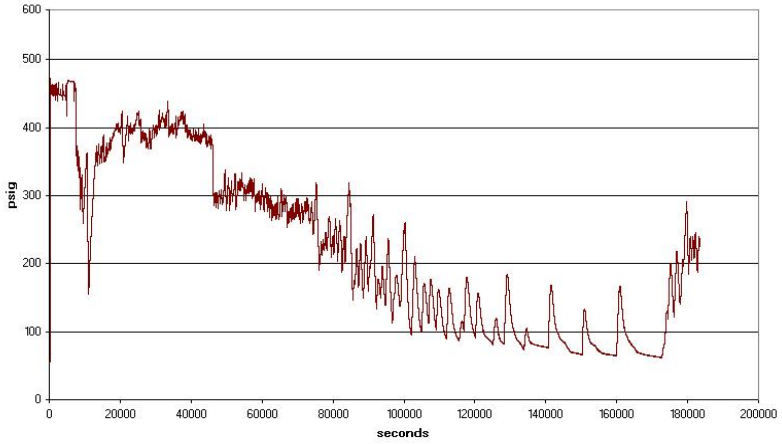


*Figure 3.6: Example result (inlet pressure) of nitrogen-water relative permeability experiment with constant gas and water flowrates.*

To remedy the problem the nitrogen inflow control was changed to constant pressure. Figure 3.7, Figure 3.8 and Figure 3.9 show the inlet pressures, nitrogen inlet flowrates, and cumulative mass of water at the outlet, respectively.

Nitrogen flowrates at the outlet are approximately constant at 0.012 ml/min. The outlet pressures are constant at 10.98 psig.

The water saturation, as determined from the resistivity-saturation correlation, is 65%.

## 3.4 CONTINUING AND FUTURE WORK

The next step is to achieve more stable steady-state results and to repeat the experiment using different gas-water ratios to achieve different core saturations.

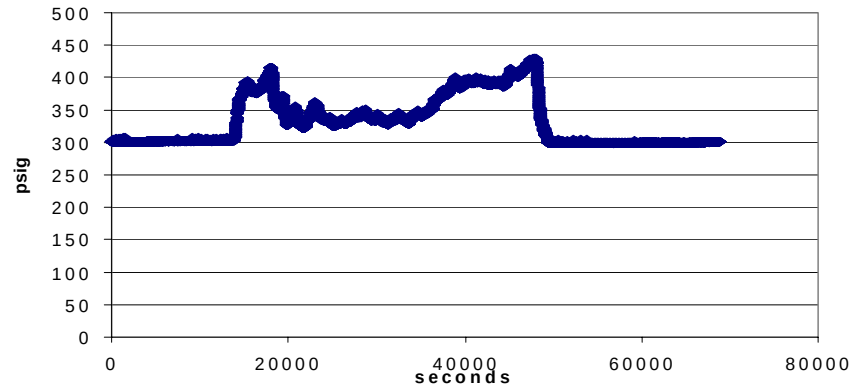


*Figure 3.7: Inlet pressure for nitrogen-water relative permeability experiment.*

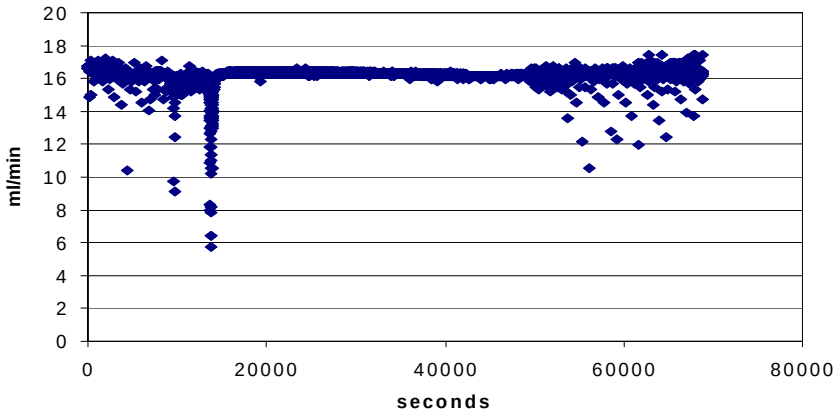


Figure 3.8: Nitrogen inlet flowrate for nitrogen-water relative permeability experiment.

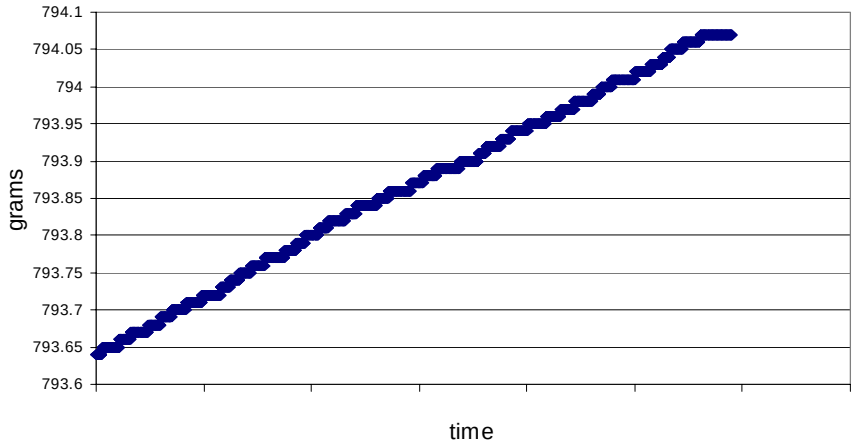


*Figure 3.9: Cumulative mass of water at the outlet. Data points shown are for last 600 seconds only.*

# 4. SCALING OF SPONTANEOUS IMBIBITION IN GAS-WATER-ROCK SYSTEMS

This research project was conducted by Research Associate Kewen Li and Professor Roland Horne. The goal of this study was to develop a method to scale the experimental data of spontaneous water imbibition for gas (steam)-water-rock.

## 4.1 SUMMARY

A method has been developed to scale the experimental data of spontaneous water imbibition (cocurrent) for gas-liquid-rock systems. In this method, a dimensionless time has been defined with the effects of relative permeability, wettability, and gravity included. The definition was not empirical but based on a theoretical derivation. Using this dimensionless time, experimental data from spontaneous water imbibition in different rocks with different size, porosity, permeability, initial water saturation, interfacial tension, and wettability could be scaled. The scaling model proposed in this study for gas-liquid-rock systems was verified experimentally for different rocks (Berea, chalk, and graywacke from The Geysers) with significantly different properties; it was also verified experimentally at different initial water saturations in the same rock. The scaling results from this study demonstrated that the cocurrent spontaneous water imbibition in gas-liquid-rock systems could be scaled and predicted.

## 4.2 INTRODUCTION

Spontaneous water imbibition is an important mechanism during water injection or aquifer invasion into highly fractured geothermal reservoirs. The amount and the rate of water imbibition from the fracture into the matrix by spontaneous imbibition are essential to the understanding of reservoir performance. The process of spontaneous water imbibition is controlled by the properties of the porous medium, fluids, and their interactions. These parameters are porosity, permeability, pore structure, matrix size and shape, boundary condition, fluid viscosity, initial water saturation, wettability, interfacial tension, relative permeability, and gravity. Li and Horne (2001d) derived an equation to correlate the imbibition rate and the recovery by considering almost all these variables.

Scaling spontaneous water imbibition is important to evaluate the production performance because so many factors are involved. In order to scale the experimental data successfully, it may be necessary to consider the effects of all the significant factors. Scaling has been investigated widely in oil-water systems but rarely in gas-liquid (steam-water) systems.

It is difficult to scale the experimental data of spontaneous imbibition in gas-liquid systems. Ignoring the effects of relative permeability, wettability, and gravity in the dimensionless time might be the reason. Natural gas-liquid-rock systems are usually strongly liquid-wet. However this does not imply that there are no significant differences among different gas-liquid-rock systems in terms of wettability. Gravity may also play an important role in some cases.

Dimensionless time used to scale spontaneous imbibition data is usually defined as follows (Ma *et al.*, 1995):

$$t_D = \sqrt{\frac{k}{\phi}} \frac{\sigma}{\mu_m L_a^2} t \tag{4.1}$$

where $t_D$ is the dimensionless time, $k$ is the rock permeability, $\phi$ is the porosity, $\sigma$ is the interfacial tension between oil and water, $t$ is the imbibition time, $\mu_m$ is the geometric mean of water and oil viscosities and $L_a$ is the characteristic length defined as follows:

$$L_a = \sqrt{\frac{V}{\sum_{i=1}^{n} \frac{A_i}{d_{ai}}}} \tag{4.2a}$$

where $V$ is the bulk volume of the matrix, $A_i$ is the area open to imbibition in the $i$ direction, and $d_{ai}$ is the distance traveled by the imbibition front from the open surface to the no-flow boundary.

The scaling group in Eq. 4.1 was modified from Mattax and Kyte (1962) who used only the water viscosity in the scaling group but a condition for scaling was that the viscosity ratio in the laboratory tests be equal to that in the reservoirs. Ma *et al*. (1995) proposed the geometric mean of the oil and water viscosities in the scaling group. The scaling method represented by Eq. 4.1 was verified experimentally by Zhang *et al*. (1996) in strongly water-wet oil-water-rock systems using Berea sandstone core samples.

Later Tong *et al*. (2001) also verified that the spontaneous water imbibition at mixed wettability for recovery (OOIP) of mineral oil of different viscosities could be correlated satisfactorily by the square root of the geometric mean of the oil and water viscosities. However, the scaling method represented by Eq. 4.1 was rarely verified experimentally in rocks with different wettability.

Zhou *et al*. (2001) proposed another scaling group of dimensionless time with mobility terms of both wetting-phase and nonwetting-phase included. The reported scaling results of recoverable recovery were improved by using the proposed dimensionless time although still scattered.

Zhang *et al*. (1996) mentioned that the square root of the geometric mean of the wetting-phase and nonwetting-phase viscosities did not scale results in gas-liquid-rock systems. Eq. 4.2 was modified from the shape factor suggested by Kazemi *et al*. (1989) As pointed out by Zhang *et al*. (1996), when the dimensionless time defined in Eq. 4.1 was used to scale the experimental data in gas-liquid systems, the results were scattered significantly.

To scale the experimental results of spontaneous oil imbibition in gas-oil systems, Wang (1999) calculated the average value of oil and gas viscosities using a different way than the geometric mean. The equation is expressed as follows:

$$\mu_m = \mu_o^{3/4}\mu_a^{1/4} \tag{4.2b}$$

where $\mu_o$ and $\mu_a$ are the viscosities of oil and air respectively. Eq. 4.2b is an empirical correlation and may have limited application, as stated by Wang (1999).

Li and Horne (2001d) recently developed a method to characterize the process of spontaneous water imbibition into gas-saturated rocks. The effects of relative permeability, capillary pressure, wettability (including in capillary pressure and relative permeability), and the gravity on the spontaneous water imbibition were considered in this model. A linear relationship between the water imbibition rate and the reciprocal of recovery by spontaneous imbibition was found and confirmed both theoretically and experimentally. The end-point relative permeability of the water-phase and the capillary pressure can be calculated simultaneously using the linear relationship. On the basis of the previous study, a method was developed to scale the experimental data of spontaneous imbibition (cocurrent) for gas-liquid systems. We defined a new dimensionless time for scaling in which effective permeability instead of absolute permeability was used. Also considered in the new dimensionless time are the capillary pressure and gravity forces.

Spontaneous water imbibition tests were conducted in gas-saturated rocks. The scaling method proposed in this study was verified experimentally by the data from different rocks (Berea, chalk, and graywacke from The Geysers geothermal field) with different size, porosity, permeability, initial water saturation, and wettability.

## 4.3 THEORY

A scaling model for gas-liquid-rock systems was derived theoretically based on the solution to the recovery by spontaneous water imbibition. The imbibition model by Li and Horne (2001d) was originally developed to characterize the spontaneous water imbibition into gas-saturated porous media and to simultaneously calculate the end-point relative permeability of the water-phase and the capillary pressure. Nonetheless this model may also be used to conduct scaling. As stated previously, the model reveals a linear relationship between the imbibition rate and the reciprocal of the gas recovery by spontaneous water imbibition and is expressed as follows:

$$Q_w = \frac{dN_{wt}}{dt} = a\frac{1}{R} - b \tag{4.3}$$

where $Q_w$ is the volumetric rate of water imbibition, $N_{wt}$ is the accumulative volume of water imbibed into rocks, $R$ is the recovery in terms of pore volume and is equal to $N_{wt}/V_p$ ($V_p$ is the pore volume). $a$ and $b$ are two constants associated with capillary and gravity

forces respectively. Note that this equation was derived based on a reasonable assumption that the mobility of the gas phase was infinite compared to the water phase.

The values of *a* and *b* can be calculated from the spontaneous water imbibition data using Eq. 4.3. The details of the calculation of *a* and *b* were presented in Li and Horne (2001d). To develop the scaling model, we need to know what the two constants represent. Constant *a* is expressed as follows:

$$a = \frac{Ak_w(S_{wf} - S_{wi})}{\mu_w L} P_c \tag{4.4}$$

where *A* and *L* are the cross-section area and the length of the core respectively, $\mu_w$ is the viscosity of water, $S_{wi}$ is the initial water saturation and $S_{wf}$ is the water saturation behind the imbibition front; $k_w$ is the effective permeability of water phase at a water saturation of $S_{wf}$. Similarly, $P_c$ is the capillary pressure at $S_{wf}$.
Constant *b* is expressed as follows:

$$b = \frac{Ak_w}{\mu_w} \Delta\rho g \tag{4.5}$$

where $\Delta\rho$ is the density difference between water and gas and *g* is the gravity constant.
To obtain the relationship between the recovery and the imbibition time from Eq. 4.3, the ratio of *b*/*a*, the normalized reovery, and the dimensionless time are defined as follows:

$$c = \frac{b}{a} \tag{4.6}$$

$$R^* = cR \tag{4.7}$$

$$t_d = c^2 \frac{k_w}{\phi} \frac{P_c}{\mu_w} \frac{S_{wf} - S_{wi}}{L_a^2} t \tag{4.8}$$

where *c* is the ratio of the gravity force to the capillary force, $t_d$ is the dimensionless time with gravity and capillary forces included. $R^*$ is the normalized recovery. In the cocurrent spontaneous water imbibition case in this study, $L_a$ is equal to the core length.

Substituting Eqs. 4.6, 4.7, and Eq. 4.8 into Eq. 4.3, the following equation is obtained:

$$\frac{R^* dR^*}{dt_d} = 1 - R^* \tag{4.9}$$

We found experimentally that $R^*$ was less than 1.0 in most cases. Therefore, the solution of Eq. 4.9 is:

$$\ln(1-R^*)+R^* = -t_d \tag{4.10}$$

Eq. 4.10 could also be expressed as follows:

$$(1-R^*)e^{R^*} = e^{-t_d} \tag{4.11}$$

We can see from Eq. 4.11 that $R^*$ is only a function of the newly defined dimensionless time. This feature shows that experimental data from spontaneous water imbibition in rocks with different size, porosity, permeability, initial water saturation, interfacial tension, and wettability can be scaled to a single curve of $R^*$ vs. $t_d$.

The procedure to scale the spontaneous water imbibition using the new method is described briefly in the following. The water imbibition rate is first plotted vs. the reciprocal of the recovery (amount of water imbibed into the gas-saturated rock in terms of pore volume). A straight line is expected from which the values of the two constants *a* and *b* could be obtained from linear regression analysis (see Ref. 1 for more detail on obtaining the two constants *a* and *b*). The effective permeability, $k_w$, and the capillary pressure, $P_c$, at $S_{wf}$ could also be calculated once the values of *a* and *b* are available. Therefore the dimensionless time defined in Eq. 4.8 and the normalized recovery defined in Eq. 4.7 could be computed. At last the normalized recovery is plotted vs. the new dimensionless time. According to Eq. 4.11, the experimental data of spontaneous water imbibition in different rocks with different specific properties is expected to correlate satisfactorily in the form of the normalized recovery vs. the new dimensionless time.

The most frequently used models in the past to characterize the spontaneous water imbibition may be the Handy model (1960) and the Aronofsky model (1958). The relationship between the two models and the model (see Eq. 4.11) developed in this study based on the Li and Horne (2001d) equation is discussed in this section. We first discuss the relationship between the Aronofsky model (1958) and the model expressed by Eq. 4.11. The term $e^{R^*}$ is close to 1 when $R^*$ is small enough. Therefore, Eq. 4.11 is reduced as follows:

$$R^* = 1-e^{-t_d} \tag{4.12}$$

Eq. 4.12 is similar to the form of an imbibition model suggested by Aronofsky *et al.* (1958). This demonstrates that our model includes the Aronofsky model (1958).

Next we discuss the relationship between the Handy model (1960) and our model. It is known that:

$$\ln(1-R^*) = -R^* - \frac{1}{2}(R^*)^2 - \frac{1}{3}(R^*)^3 - \cdots \tag{4.13}$$

Substituting Eq. 4.13 into Eq. 4.10 after neglecting the third- and the greater-order terms, the following expression can be obtained:

$$(R^*)^2 = 2t_d \tag{4.14}$$

According to Eqs. 4.4-4.8, Eq. 4.14 can be deduced as follows:

$$N_{wt}^2 = \frac{2P_c k_w \phi (S_{wf} - S_{wi}) A^2}{\mu_w} t \tag{4.15}$$

Eq. 4.15 is similar to the Handy equation (1960). The only difference between the two is that initial water saturation is not included in the Handy equation (1960).

According to the analysis in the previous section, we can see that the imbibition model (see Eq. 4.11) developed in this study based on the Li and Horne equation (2001) is more generalized. This is because our model includes both the Handy model (1960) and the Aronofsky model (1958).

## 4.4 EXPERIMENTAL

Spontaneous water imbibition experiments in air-saturated chalk were performed in this work. Li and Horne (2000, 2001) previously conducted spontaneous water imbibition (cocurrent experiments) in the rocks (graywacke) from The Geysers and in Berea sandstone with clay removed by firing. These experimental data and others were used to verify the scaling method developed in this study.

Air was used as the gas phase and distilled water as the liquid phase because the clay in the Berea sandstone core was deactivated by firing. The surface tension of water/air at 20$^o$C is 72.75 dynes/cm.

The permeability of the chalk sample was around 5 md; its length and diameter were 7.5 cm and 2.54 cm, respectively.

The natural (clay was not removed by firing) Berea sandstone sample had an air permeability of around 804 md and a porosity of about 21.2%; its length and diameter were 9.962 cm and 4.982 cm.

Another Berea sandstone sample was fired at a temperature of 600$^o$C to remove the clay and had a permeability of around 1200 md and a porosity of about 24.5%; its length and diameter were 43.5 cm and 5.06 cm.

The Geysers rock sample from a depth of 1410.1m was obtained from the Energy and Geoscience Institute; its porosity was about 4.5%. The matrix permeability of the rock sample is not available yet. The permeability of a nearby sample measured by nitrogen injection was about 0.56 md (after calibration of gas slip effect), which is probably attributable mainly to the fracture permeability. The length and diameter of this rock sample were 3.52 cm and 8.25 cm.

## 4.5 RESULTS

The experimental data of spontaneous water imbibition (cocurrent) in different rocks at different initial water saturations were used to confirm the scaling method proposed in this study. The analysis and discussion is presented in this section.

### 4.5.1 Scaling for Different Values of Initial Water Saturation in Fired Berea

To verify the scaling approach, the experimental data from Li and Horne (2001d), who conducted cocurrent spontaneous water imbibition experiments at different initial water saturations in the Berea sandstone, were used. As mentioned previously, the Berea sandstone was fired to deactivate the clay. The amounts of water imbibed into the air-saturated Berea sandstone were measured at three initial water saturations and the results are shown in Fig. 4.1. The lower the initial water saturation, the more the water imbibed into the core sample.

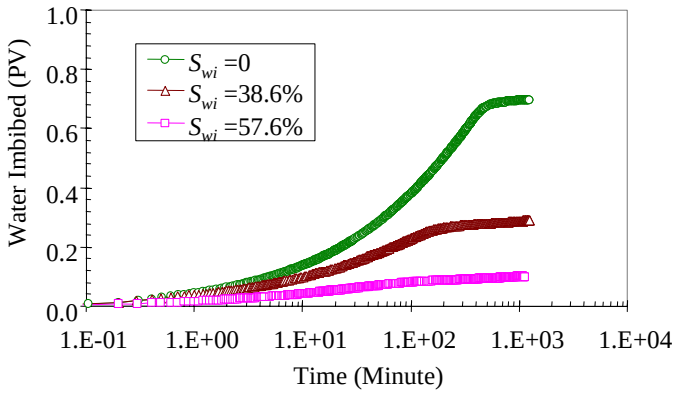


*Figure 4.1: Spontaneous water imbibition behavior in fired Berea sandstone.*

Using the existing dimensionless time defined in Eq.1, the scaling results for the spontaneous water imbibition data at three different initial water saturations (see Fig. 4.1) are shown in Fig. 4.2. Different researchers use different definitions of recovery. Some use recovery in terms of original reserves in place and others use recovery in terms of recoverable reserves. In this paper we present the results using the two definitions. Fig. 4.2a shows the relationship between the recovery in terms of gas originally in place (GOIP) and the existing dimensionless time; Fig. 4.2b shows the relationship between the recovery in terms of recoverable reserves and the existing dimensionless time. Note that only water viscosity was used in the scaling. The geometric mean viscosity term in Eq. 4.1 was substituted by the viscosity of water. It is supposed that all the experimental data points obtained at different initial water saturations should sit close to a single curve if

the dimensionless time is appropriate for the scaling. However, Figs. 4.2a and 4.2b demonstrate that the experimental data points scatter significantly.

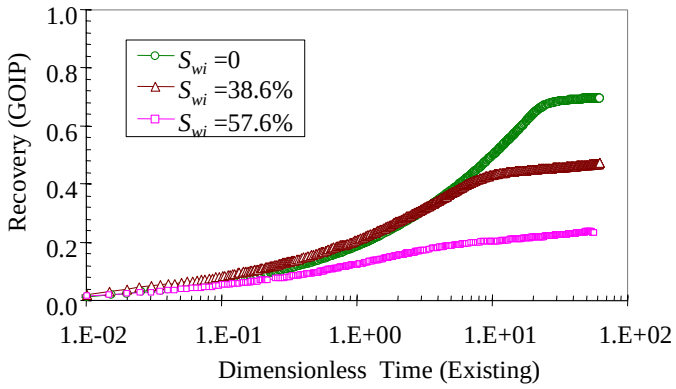


(a) Recovery in terms of GOIP

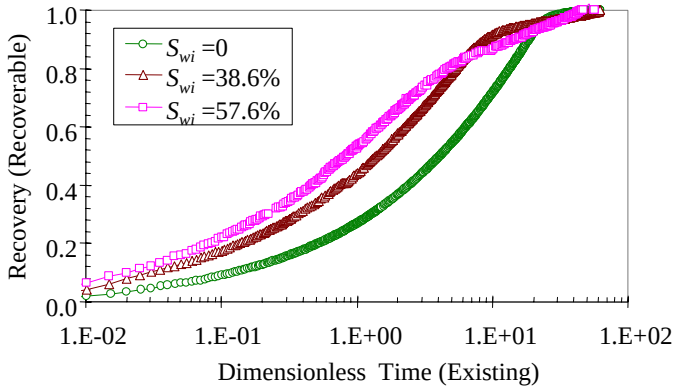


(b) Recovery in terms of recoverable reserves

*Figure 4.2: Scaling using existing dimensionless time for fired Berea sandstone at different initial water saturations.*

Using the scaling method developed in this study (see Eqs. 4.7 and 4.8), the same experimental data presented in Fig. 4.2 were plotted as the normalized recovery versus the new dimensionless time and the results are shown in Fig. 4.3. All the experimental data of the spontaneous water imbibition sit in a single curve except those after the water imbibition front reached the top of the core. We can see from Fig. 4.3 that the proposed scaling model works remarkably well for the spontaneous water imbibition in the fired Berea sandstone for different initial water saturations.

The normalized recovery by spontaneous water imbibition is supposed to be less than one. However, some values of the normalized recovery at the initial water saturation of 57.8% are greater than one after the water imbibition front reached the top of the core sample. Evaporation of the water may be the cause for this. At high initial water saturation, the calculated values of the normalized recovery are very sensitive to error of measurements of water imbibed. Experimental results from a shorter Berea core sample

were also used to conduct the scaling. The water evaporation in a shorter core sample is expected to be less and the scaling results should then be less scattered in the later time of experiment. This will be discussed in more detail in the next section.

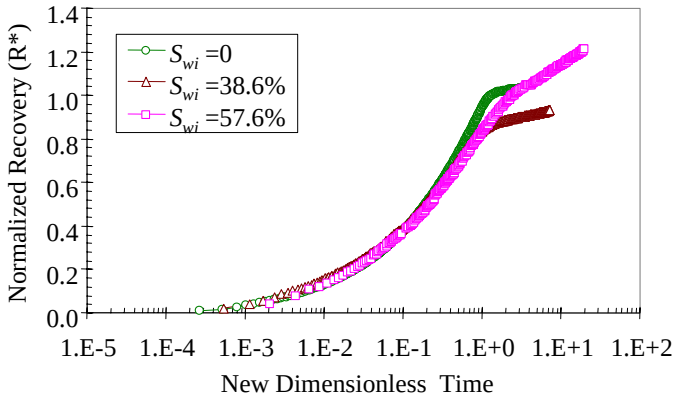


*Figure 4.3: Scaling using new dimensionless time for fired Berea sandstone at different initial water saturations.*

## 4.5.2 Scaling for Different Values of Initial Water Saturation in Natural Berea without Clay Removed

Spontaneous water imbibition (cocurrent) tests in natural Berea sandstone without clay removed were conducted by Chow *et al*. (1999). Compared to the fired Berea sandstone sample, the natural one had lower permeability and smaller size. The wettability might also be significantly different. The relationships between the amounts of water imbibed into the Berea sandstone and the time at five different initial water saturations are shown in Fig. 4.4. As in the fired Berea sandstone, the amount of water imbibed decreases with an increase of initial water saturation.

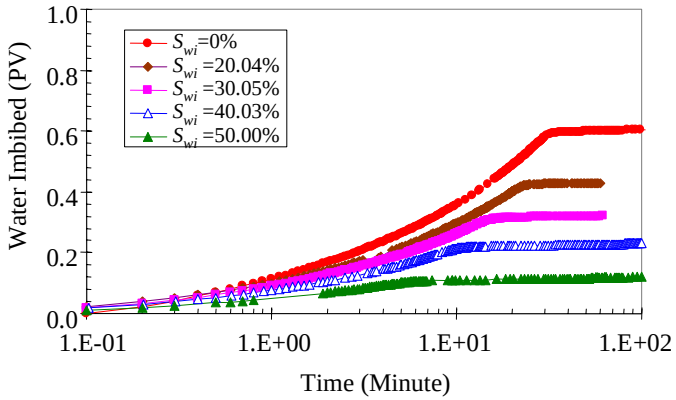


*Figure 4.4: Spontaneous water imbibition behavior in natural Berea sandstone.*

Fig. 4.5 shows the scaling results for the spontaneous water imbibition data at five different initial water saturations using the existing dimensionless time defined in Eq.1. As before, only water viscosity was used in the scaling. Fig. 4.5a represents the recovery

in terms of GOIP. The experimental data points before the imbibition front touched the top of the core sample could be scaled but the points measured later scatter significantly.

Fig. 4.5b shows scaling results in terms of recoverable recovery using the existing scaling model for the same experimental data used in Fig. 4.5a. The data points before the imbibition front touched the top of the core sample are scattered but those measured later could be scaled except the point at the initial water saturation of 50%.

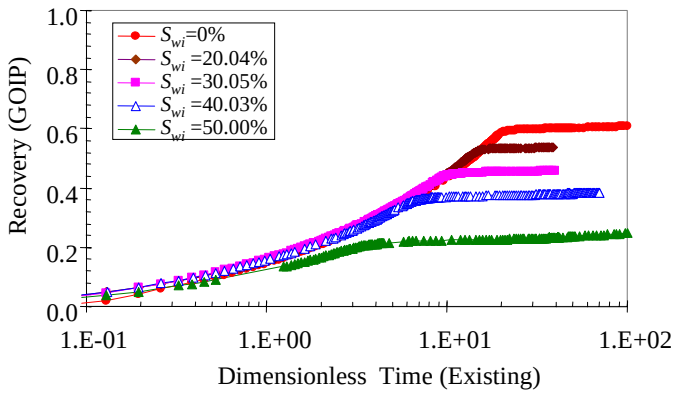


(a) Recovery in terms of GOIP

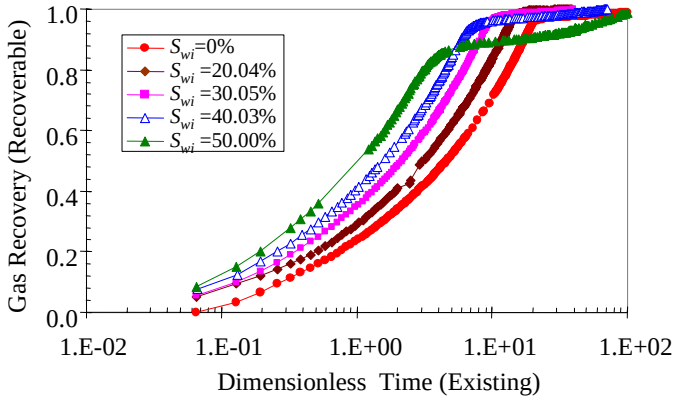


(b) Recovery in terms of recoverable reserves

*Figure 4.5: Scaling using existing dimensionless time for natural Berea sandstone at different initial water saturations.*

Using the normalized recovery defined in Eq. 4.7 and the scaling dimensionless time defined in Eq. 4.8, the same experimental data shown in Fig. 4.5 were replotted and the results are shown in Fig. 4.6. The proposed scaling model (Eqs. 4.7 and 4.8) works extraordinarily well for the spontaneous water imbibition in natural Berea sandstone at five different values of initial water saturation for all the experimental data, both before and after the imbibition front of water touched the top of the core sample.

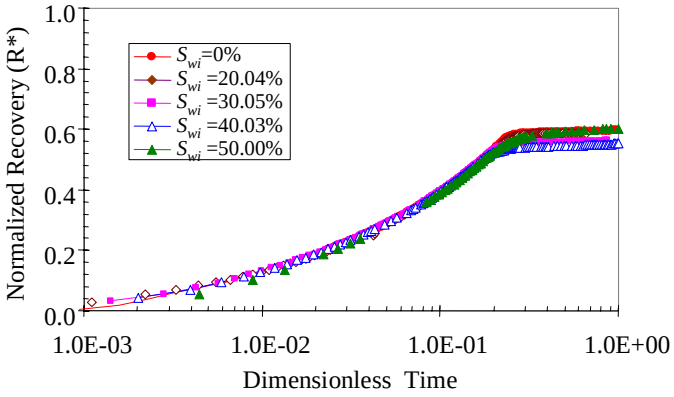


*Figure 4.6: Scaling using the new scale model for Berea sandstone at different initial water saturations.*

The scaling results presented in Fig. 4.6 show that a single satisfactory correlation between the normalized recovery defined in Eq. 4.7 and the scaling dimensionless time defined in Eq. 4.8 may be obtained.

### 4.5.3 Scaling in Different Rocks

Capillary pressures and relative permeabilities (the effect of wettability may be represented by the two factors) may be different in different rocks. So the spontaneous water imbibition behavior would not be the same. The relationships between the amount of water imbibed into different rocks (fired Berea sandstone, natural Berea sandstone, chalk, and the graywacke from The Geysers geothermal field) and the imbibition time are shown in Fig. 4.7. Berea_1 and Berea_2 in Fig. 4.7 represent the fired Berea sandstone and the natural Berea sandstone respectively. We can see from Fig. 4.7 that the behavior of the spontaneous water imbibition in different rocks is much different. The imbibition rate and the ultimate recovery obviously depend on the rock properties. We can also see from Fig. 4.7 that firing the Berea sandstone significantly altered the behavior of the spontaneous water imbibition.

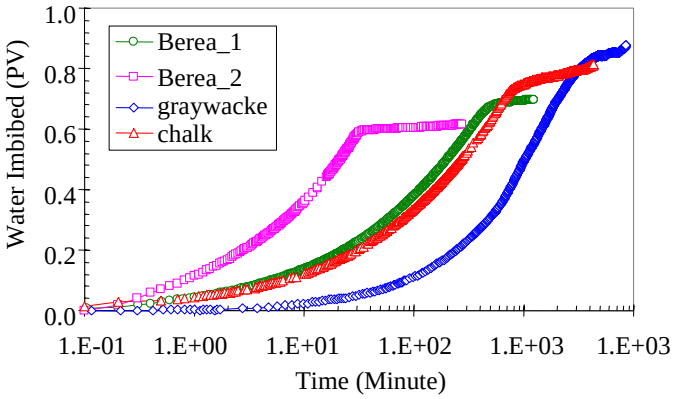


*Figure 4.7: Spontaneous water imbibition behavior in four different rocks.*

Investigations on scaling of spontaneous water imbibition in different rocks have been infrequent. Figs. 4.8a and 4.8b show the scaling results for the spontaneous water imbibition data in different rocks using the existing scaling group of dimensionless time defined in Eq. 4.1. The existing scaling model does not work well for the spontaneous water imbibition in different rocks for the experimental data both before and after the imbibition front touched the top of the core sample. Different rocks may have different wettability, capillary pressure, relative permeability, and so on. However, these factors are not included in the existing scaling model. This may be why the existing scaling model could not scale experimental data of spontaneous water imbibition in different rocks.

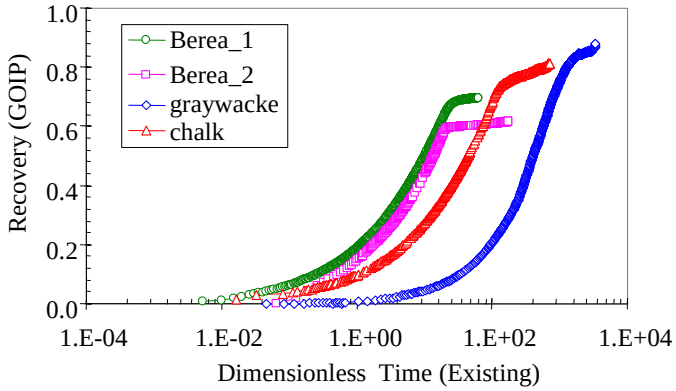


(a) Recovery in terms of GOIP

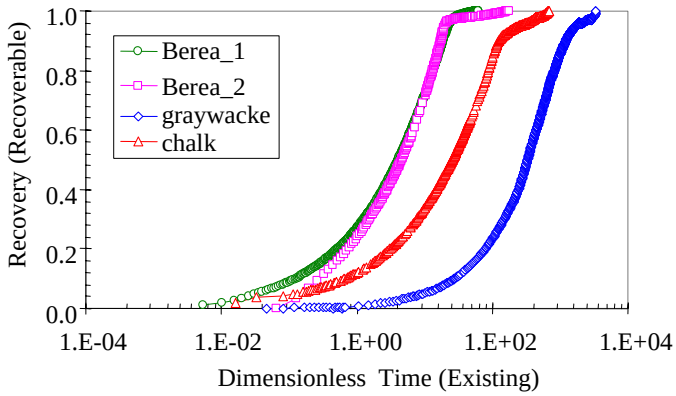


(b) Recovery in terms of recoverable reserves

*Figure 4.8: Scaling using existing dimensionless time for different rocks.*

The experimental data in different rocks (the same as in Fig. 4.8) were grouped using the normalized recovery $R^*$ and our scaling dimensionless time $t_d$. The scaling results in different rocks are shown in Fig. 4.9. The proposed scaling model works satisfactorily for the spontaneous water imbibition in different rocks with very different properties, although it does not scale the results after the imbibition front touched the top of the core sample.

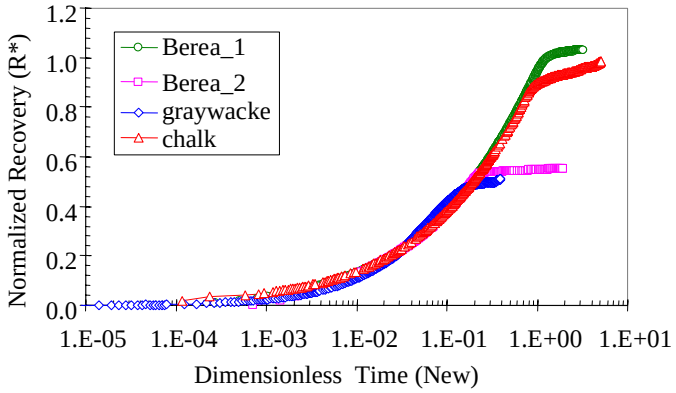


*Figure 4.9: Scaling using the new scale model for different rocks.*

### 4.5.3 Scaling for All Experimental Results Studied

Fig. 4.10a shows the relationship between the recovery in terms of gas originally in place and the existing dimensionless time for all the experimental data (available to us) of spontaneous water imbibition in different rocks and at different initial water saturations. Fig. 4.10b plots the same experimental data of the recovery in terms of recoverable reserves. We can see from both Fig. 4.10a and Fig. 4.10b that the data points obtained by existing scaling model significantly scatter for the spontaneous water imbibition in different rocks and at different initial water saturations.

Fig. 4.11 shows the results using the scaling model developed in this study (see Eqs. 4.7 and 8). Our scaling model achieved an acceptable correlation between the normalized recovery and the new scaling dimensionless time for the experimental data before the imbibition front touched the top of the core sample.

## 4.6 DISCUSSION

One of the distinguishing features of the newly developed scaling model for gas-liquid-rock systems is that almost all the factors involved in cocurrent spontaneous water imbibition, including porosity, permeability, pore structure, matrix size, fluid viscosity, initial water saturation, wettability, interfacial tension, relative permeability, and gravity, were considered. Another feature is that this scaling model was derived according to the fluid flow mechanisms in porous media instead of by empirical analysis.

The scaling model was confirmed experimentally at different initial water saturations in the same rock (fired and natural Berea sandstone samples respectively). The initial water saturation ranged from 0 to about 57%. This model was also confirmed in rocks with different porosity, permeability, and size. The permeability varied in the range from less than one md to more than 1000 md.

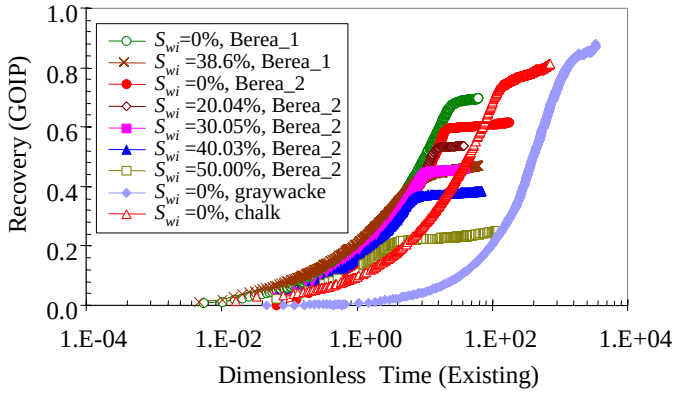


(a) Recovery in terms of GOIP

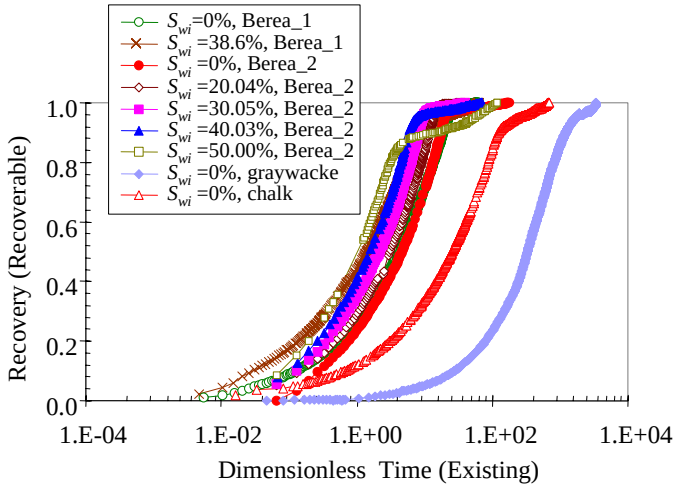


(b) Recovery in terms of recoverable reserves

*Figure 4.10: Scaling using the existing dimensionless time for all experimental results studied.*

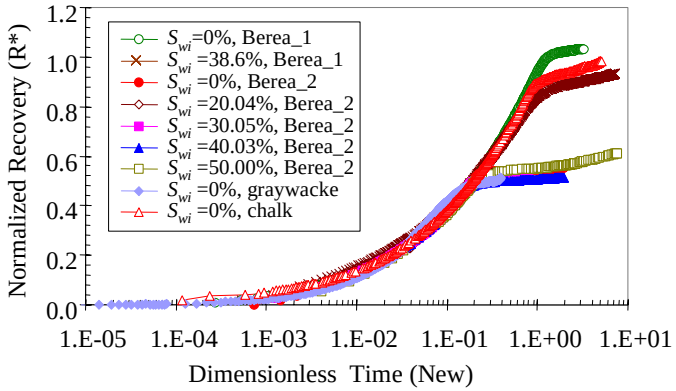


*Figure 4.11: Scaling using the new scale model for rocks with very different property at different initial water saturations.*

There are not many experimental results of cocurrent spontaneous water imbibition in gas-liquid-rock systems available in the literature. The scaling model proposed in this study may need to be further verified if more experimental data become available although it works very well for the experimental results presented.

The approach used in this study to develop the scaling model could be deployed to gain a general scaling model to scale the experimental data of spontaneous imbibition in almost any system such as oil-gas-rock, gas-water-rock, and oil-water-rock systems in both cocurrent and countercurrent spontaneous imbibition cases. We have done the theoretical derivation and achieved such a general scaling model. The corresponding experiments are being conducted and the results will be published in a later paper.

## 4.7 CONCLUSIONS

The following conclusions may be drawn according to our present study:

1. A method was developed based on the theory of fluid flow instead of empiricism. This method may be used to scale the experimental data of cocurrent spontaneous imbibition in gas-liquid-rock systems.
2. The dimensionless time was defined with initial water saturation, relative permeability, capillary pressure (instead of only interfacial tension), wettability, and gravity included. It is known that these factors have a significant effect on cocurrent spontaneous imbibition.
3. The scaling model proposed in this study for gas-liquid-rock systems was verified experimentally for rocks with different porosity, permeability, size, and other different properties.
4. The scaling model works remarkably well at different initial water saturations in the same rock both before and after the imbibition front contacted the top of the core sample.
5. A correlation between the normalized recovery and the new dimensionless time was obtained for all the present experimental data of spontaneous water imbibition in different rocks before the imbibition front contacted the top of the core sample.
6. A more generalized imbibition model was derived in this study to correlate the normalized recovery and the dimensionless time; this model encompasses both the Handy model and the model suggested by Aronofsky *et al*.

## 5. REFERENCES


Aronofsky, J.S., Masse, L., and Natanson, S.G.: " A Model for the Mechanism of Oil Recovery from the Porous Matrix Due to Water Invasion in Fractured Reservoirs," *Trans*. AIME (1958) **213**, 17-19.

Beckner, B.L., Firoozabadi, A., and Aziz, K.: "Modeling Transverse Imbibition in Double-Porosity Simulators", SPE 17414, presented at the 1988 SPE California Regional Meeting, Houston, Long Beach, USA, March 23-25, 1988.

Brooks, R. H. and Corey, A. T.: "Properties of Porous Media Affecting Fluid Flow", *J. Irrig. Drain. Div*., (1966), **6**, 61.

Burdine, N. T.: "Relative Permeability Calculations from Pore Size Distribution Data", *Trans. AIME*, (1953), **198**, 71.

Chow, K., Li, K., and Horne, R. N. (1999): Quarterly Report for October-December 1999, Stanford Geothermal Program, DE-FG07-95ID13763.

Corey, A.T., "The Interrelations Between Gas and Oil Relative Permeabilities," *Producers Monthly* Vol. 19 (1954), pp 38-41.

Diomampo, G., " Relative Permeability through Fracture", MS thesis, Stanford University, Stanford, California (2001).

Fatt, I. and Dykstra, H.: "Relative Permeability Studies", *Trans. AIME*, (1951), **192**, 249.

Fourar, M. and Bories, S.,: "Experimental Study of Air-Water Two-Phase Flow Through A Fracture (Narrow Channel)," *Int. J. Multiphase Flow* Vol. 21, No. 4, Toulouse, France (1995) pp. 621-637.

Fourar, M., Bories., Lenormand, R., and Persoff, P.,: "Two-Phase Flow in Smooth and Rough Fractures: Measurement and Correlation by Porous-Medium and Pipe Flow Models," *Water Resources Research* Vol. 29 No. 11. November 1993, pp. 3699-3708.

Gates, J. I. and Leitz, W. J.: "Relative Permeabilities of California Cores by the Capillary Pressure Method", paper presented at the API meeting, Los Angeles, California, May 11, 1950, 286.

Handy, L.L.: "Determination of Effective Capillary Pressures for Porous Media from Imbibition Data," Petroleum Transactions AIME, Vol. 219, 1960, 75-80.

Honarpour, M. M., Koederitz, L., and Harvey, A. H.: *Relative Permeability of Petroleum Reservoirs*, *CRC* press, Boca Raton, Florida, USA, 1986, ISBN 0-8493-5739-X, 19.

Horne, R.H., Satik, C., Mahiya, G., Li, K., Ambusso, W., Tovar, R., Wang, C., and Nassori, H.: "Steam-Water Relative Permeability," *Proc. of the World Geothermal Congress* 2000, Kyushu-Tohoku, Japan, May 28-June 10, 2000.

Huang, D. D., Honarpour, M. M., Al-Hussainy, R.: "An Improved Model for Relative Permeability and Capillary Pressure Incorporating Wettability", SCA 9718, Proceedings of International Symposium of the Society of Core Analysts, Calgary, Canada, September 7-10, 1997.

Kazemi, H., Gilman, J.R., and El-Sharkaway, A.M.: "Analytical and Numerical Solution of Oil Recovery from Fractured Reservoirs Using Empirical Transfer Functions," paper SPE 19849, presented at the SPE 64th Annual Technical Conference and Exhibition, San Antonio, TX, October 8-11, 1989.

Kleppe, J. and Morse, R. A.: "Oil Production from Fractured Reservoirs by Water Displacement," SPE 5084, presented at the 1974 SPE Annual Technical Conference and Exhibition, Houston, TX, USA, October 6-9, 1974.

Kneafsy, T. J. and Pruess, K.,: "Laboratory Experiments on Heat-Driven Two-Phase Flows in Natural and Artificial Rock Fractures," *Water Resources Research* Vol. 34, No. 12, December 1998, pp. 3349-3367.

Land, C. S.: "Calculation of Imbibition Relative Permeability for Two- and Three-Phase Flow from Rock Properties", *SPEJ*, (June 1968), 149.

Land, C. S.: "Comparison of Calculated with Experimental Imbibition Relative Permeability", *Trans. AIME,* (1971), **251**, 419.

Li, K., and Horne, R.N., "Accurate Measurement of Steam Flow Properties," *GRC Transactions* 23 (1999).

Li, K. and Horne, R.N.: "An Experimental Method for Evaluating Water Injection into Geothermal Reservoirs," presented at the GRC 2000 annual meeting, September 24-27, 2000, San Francisco, USA; *GRC* Trans. V. **24**.

Li, K. and Horne, R.N. (2001a): "An Experimental Method of Measuring Steam-Water and Air-Water Capillary Pressures," paper 2001-84, presented at the Petroleum Society's Canadian International Petroleum Conference 2001, Calgary, Alberta, Canada, June 12–14, 2001.

Li, K. and Horne, R.N. (2001b): "An Experimental and Analytical Study of Steam/Water Capillary Pressure," *SPEREE* (December 2001), 477-482.

Li, K. and Horne, R.N. (2001c): "Gas Slippage in Two-Phase Flow and the Effect of Temperature," SPE 68778, presented at the 2001 SPE Western Region Meeting, Bakersfield, CA, USA, March 26-30, 2001.

Li, K. and Horne, R.N. (2001d): "Characterization of Spontaneous Water Imbibition into Gas-Saturated Rocks," *SPEJ* (December 2001), **6**(4), 375.

Lockhart, R. W. and Martinelli, R.C.,: "Proposed Correction of Data for Isothermal two-phase component flow in pipes," *Chem. Eng. Prog*., Vol. 45, No. 39, 1949.

Ma, S., Morrow, N.R., and Zhang, X.: "Generalized Scaling of Spontaneous Imbibition Data for Strongly Water-Wet Systems," paper 95-138, presented at the 6th

Petroleum Conference of the South Saskatchewan Section, the Petroleum Society of CIM, held in Regina, Saskatchewan, Canada, October 16-18, 1995.

Mahiya, G., "Experimental Measurement Of Steam-Water Relative Permeability," MS thesis, Stanford University, Stanford, California (1999).

Mattax, C.C. and Kyte, J.R.: "Imbibition Oil Recovery from Fractured, Water-Drive Reservoir," *SPEJ* (June 1962), 177-184.

Pan, X., Wong, R.C., and Maini, B.B.: Steady State Two-Phase Flow in a Smooth Parallel Fracture, presented at the 47th Annual Technical Meeting of the Petroleum Society in Calgary, Alberta, Canada, June 10-12, 1996.

Persoff, P. K., Pruess, K. and Myer, L.: "Two-Phase Flow Visualization and Relative Permeability Measurement in Transparent Replicas of Rough-Walled Rock Fractures," *Proc. 16th Workshop on Geothermal Reservoir Engineering*, Stanford University, Stanford, California, January 23-25, 1991

Persoff, P., and Pruess, K.: "Two-Phase Flow Visualization and Relative Permeability Measurement in Natural Rough-Walled Rock Fractures," *Water Resources Research* Vol. 31, No. 5, May, 1995, pp. 1175-1186.

Pruess, K., and Tsang, Y. W.: "On Two-Phase Relative Permeability and Capillary Pressure of Rough-Walled Rock Fractures," *Water Resources Research* Vol. 26 No. 9, September 1990, pp 1915-1926.

Purcell, W.R.: "Capillary Pressures-Their Measurement Using Mercury and the Calculation of Permeability", *Trans. AIME*, (1949), **186**, 39.

Rapoport, L. A. and Leas, W. J.: "Relative Permeability to Liquid in Liquid-Gas System", *Trans. AIME*, (1951), **192**, 83.

Richardson, J.G., Kerver, J.K., Hafford, J.A., and Osoba, J.S.: "Laboratory Determination of Relative Permeability ", *Trans. AIME*, (1952), **195**, 187.

Scheidegger, A.E. *The Physics of Flow Through Porous Media*, 3rd ed., University of Toronto, Toronto. 1974.

Su, G. W., Geller, J. T., Pruess, K. and Wen, F.,: " Experimental Studies of Water Seepage and Intermittent Flow in Unsaturated, Rough-Walled Fractures," *Water Resources Research*, Vol. 35, No. 4, April 1999, pp. 1019-1037.

Tong, Z., Xie, X., and Morrow, N. R.: "Scaling of Viscosity Ratio for Oil Recovery by Imbibition from Mixed-Wet Rocks," paper SCA 2001-21, proceedings of the International Symposium of the Society of Core Analysts, Edinburgh, UK, September 17-19, 2001.

Wang, R.: "Gas Recovery from Porous Media by Spontaneous Imbibition of Liquid," MS report, The University of Wyoming, Laramie, Wyoming, USA, 1999.

Witherspoon, P.A., Wang, J.S.W., Iwai, K. and Gale, J.E.: " Validity of Cubic Law for Fluid Flow in a Deformable Rock Fracture," *Water Resources Research*, Vol. 16, No. 6, 1980, pp 1016-1024.

Wyllie, M. R. and Gardner, G. H. F.: "The Generalized Kozeny-Carman Equation, Its Application to Problems of Multiphase Flow in Porous Media", *World Oil*, (1958), **146**, 121.

Zhang, X., Morrow, N.R., and Ma, S.: "Experimental Verification of a Modified Scaling Group for Spontaneous Imbibition," *SPERE* (November 1996), 280-285.

Zhou, D., Jia, L., Kamath, J., and Kovscek, A. R.: "An Investigation of Counter-Current Imbibition Processes in Diatomite," paper SPE 68837, presented at the 2001 SPE Western Regional Meeting, Bakersfield, California, March 26-30, 2001.